

# THE DISK AND DARK HALO MASS OF THE BARRED GALAXY NGC 4123. II. FLUID-DYNAMICAL MODELS

BENJAMIN J. WEINER

Observatories of the Carnegie Institution of Washington, 813 Santa Barbara St, Pasadena, CA 91101

J. A. SELLWOOD AND T. B. WILLIAMS

Department of Physics and Astronomy, Rutgers University, 136 Frelinghuysen Rd., Piscataway, NJ 08854

*Accepted to ApJ*

## ABSTRACT

We report a dynamical determination of the separate contributions of disk and dark halo masses to the rotation curve of a spiral galaxy. We use fluid-dynamical models of gas flow in the barred galaxy NGC 4123 to constrain the dynamical properties of the galaxy: disk  $M/L$ , bar pattern speed, and the central density and scale radius of the dark halo. We derive a realistic barred potential directly from the light distribution. For each model we assume a value of the stellar  $M/L$  and a bar pattern speed  $\Omega_p$  and add a dark halo to fit the rotation curve. We then compute the gas flow velocities with a 2-D gas dynamical code, and compare the model flow patterns to a 2-D velocity field derived from Fabry-Perot observations. The strong shocks and non-circular motions in the observed gas flow require a high stellar  $M/L$  and a fast-rotating bar. Models with  $I$ -band disk  $M/L$  of  $2.0 - 2.5h_{75}$ , or 80 – 100% of the maximum disk value, are highly favored. The corotation radius of the bar must be  $\leq 1.5$  times the bar semi-major axis. These results contradict some recent claimed “universal” galaxy disk/halo relations, since NGC 4123 is of modest size (rotation curve maximum  $145 \text{ km s}^{-1}$ , and  $V_{\text{flat}} = 130 \text{ km s}^{-1}$ ) yet is quite disk-dominated. The dark halo of NGC 4123 is less concentrated than favored by current models of dark halos based on cosmological simulations. Since some 30% of bright disk galaxies are strongly barred and have dust lanes indicating shock morphology similar to that of NGC 4123, it is likely that they also have high stellar  $M/L$  and low density halos. We suggest that luminous matter dominates inside the optical radius  $R_{25}$  of high surface brightness disk galaxies.

*Subject headings:* galaxies: kinematics and dynamics — galaxies: halos — galaxies: structure — hydrodynamics — dark matter

## 1. INTRODUCTION

Extended rotation curves of spiral galaxies provide the most solid evidence for mass discrepancies on galactic scales, requiring galaxies to be embedded in halos of dark matter. However, the relative contributions of disk and halo to the mass of galaxies are not well known. The rotation curve of an axisymmetric disk galaxy does not provide enough information to disentangle the disk and halo contributions to the mass distribution. Even a well-sampled and spatially extended rotation curve can be fitted well by any combination of disk and halo from no disk to a “maximum disk” value (van Albada *et al.* 1985). There is no consensus yet on whether maximum disks are preferred; we review arguments for and against in section 2. As a result, we do not know the relative importance of disk and halo, which hampers our understanding of major problems in galaxy formation and dynamics, including the efficiency of assembly of baryons into disks, the origin of the Tully-Fisher relation, and the importance of instabilities such as bars, spiral arms, and warps.

Here we show that the disk-halo degeneracy can be broken in barred galaxies. Two-dimensional velocity fields show that bars drive non-circular streaming motions (see Weiner *et al.* 2000, Paper I). The strength and location of the non-circular motions are governed by the ellipticity of the potential, hence the mass of the bar, and, to a lesser extent, by the bar pattern speed, the angular rate of figure rotation of the bar. In strongly barred galaxies, the bar is the dominant visible component in the inner galaxy, and the (unobservable) dark halo should be more

rounded than the bar. Thus the extra information in the non-circular motions can determine the mass-to-light ratio ( $M/L$ ) of the bar and, by extension, the mass of the stellar disk.

In this paper, we model the non-circular flow pattern of gas in the disk of NGC 4123, which we obtained in Paper I from optical and radio emission line observations. Since we observe only the line-of-sight velocity, we cannot reconstruct the full space velocity field of the gas, as we can for an axisymmetric galaxy. Furthermore, shocks are observed in the gas velocity field, so fluid dynamical models of the gas flow are needed. We compare these models against the observed velocity field in order to derive the disk  $M/L$ . The disk  $M/L$  determines the importance of the bar, hence the ellipticity of the potential, and thus controls the strength of non-circular motions and shocks: large shocks require a fairly non-circular potential and hence a significant contribution from the stellar bar.

We construct models for the galactic potential from our photometric observations and run fluid-dynamical simulations of the gas flow in a range of model potentials, for different disk  $M/L$  and bar pattern speeds  $\Omega_p$ . We then compare the model velocity fields to that observed to find the most likely values of  $M/L$  and  $\Omega_p$ . As in Paper I, we assume a distance to NGC 4123 of 22.4 Mpc, which is based on a Hubble constant of  $75 \text{ km s}^{-1} \text{ Mpc}^{-1}$ ; all values of  $M/L$  in this paper are implicitly followed by a factor of  $h_{75}$ .

## 2. THE DISK-HALO DEGENERACY AND MAXIMUM DISKS

Rotation curves of axisymmetric disk galaxies which extend beyond the optical disk clearly require dark matter but do not contain enough information to distinguish between disk-halo decompositions ranging from zero-mass to maximum disks (van Albada *et al.* 1985; van Albada & Sancisi 1986). The “maximum disk” hypothesis, requiring that the disk be as massive as possible, was originally invoked simply for definiteness to place a lower bound on the dark mass. We review here some arguments for and against maximal disks (see also the reviews of Bosma 1999 and Sellwood 1999).

Non-axisymmetric structure provides some information about disk  $M/L$ . Two-armed spiral patterns are common in disks, and excessive halo mass suppresses two-armed spiral structure, favoring disks 50% – 100% of maximum mass (Athanasoula, Bosma & Papaioannou 1987). The maximum disk or even “no halo” assumptions can reproduce the overall shape of the rotation curve inside the optical disk (*e.g.* Kalnajs 1983; van Albada *et al.* 1985; Kent 1986; Begeman 1987; Freeman 1992; Palunas 1996; Broeils & Courteau 1997). Small-scale “bumps and wiggles” in the rotation curve do not offer compelling support for maximum disks (van der Kruit 1995; Palunas 1996). Quillen & Frogel (1997) integrated periodic orbits in potentials for the ringed barred galaxy NGC 6782 and concluded that its disk should have an  $M/L$  of  $75 \pm 15\%$  of maximum (see also Quillen, Frogel & Gonzalez 1994 for application to a bar).

Dynamical friction from a heavy halo will slow down a bar (Weinberg 1985; Debattista & Sellwood 1998); bars are slowed down rapidly in even mildly submaximal disks. There are several reasons to believe that bars rotate quickly (see the review of Elmegreen 1996), and two bars have been observed to be fast rotators (Merrifield & Kuijken 1995; Gerssen, Merrifield & Kuijken 1999). The bar of the Milky Way is also best modeled as a fast rotator (Weiner & Sellwood 1999; Fux 1999).

Bottema (1993, 1997) has argued that stellar velocity dispersions imply that disks supply only about 63% of the maximum rotation velocity, so that disk  $M/L$  is 40% of maximum (see also Fuchs 1999). However, Bottema’s analysis rests on a chain of assumptions and the upper bound can be relaxed (Bosma 1999). While the Oort limit from the vertical stellar velocity dispersion has a long history as a measurement of disk mass (*e.g.* Oort 1932; Kuijken & Gilmore 1991) it is still unclear whether even the Milky Way disk is maximal or not (Sackett 1997; Binney & Merrifield 1998, chapter 10). Its application to external galaxies has two major complications: (1) we cannot measure both vertical scale height and vertical velocity dispersion in any individual galaxy; (2) integrated-light measurements of the vertical velocity dispersion will be dominated by young stars, which have a lower dispersion in the Milky Way (see Binney & Merrifield 1998, chapter 10; but cf. Fuchs 1999).

Maller *et al.* (2000) used gravitational lensing by an edge-on disk galaxy at  $z = 0.41$  to measure its potential, concluding that a maximal disk is ruled out, though a model with a massive bulge and sub-dominant halo is allowed. The lack of kinematic information makes attempts at rotation curve decomposition preliminary.

Courteau & Rix (1999) show that if galaxies have maximal disks, there should be a relationship between scale

length and the peak of the disk rotation curve  $V_{2.2}$ , predicting a correlation between scale length and residual from the Tully-Fisher relation  $\Delta V_{2.2}$ : smaller disks should have a higher rotation width at a given luminosity. They find no such correlation between the residuals from the velocity width–magnitude and scale length–magnitude relations, implying the disk contribution to rotation width is small.

In searching for a correlation between scale length and rotation width at a fixed luminosity, there is a surface brightness dependence: larger disks will have lower surface brightness. As Courteau & Rix note, the lack of correlation demonstrates that surface brightness is not a second parameter in the TF relation. LSB disks do indeed lie on the same TF relation as HSB disks (Zwaan *et al.* 1995; Sprayberry *et al.* 1995), although a “baryonic TF” relation may be required (McGaugh *et al.* 2000; O’Neil, Bothun & Schombert 2000). Lower surface brightness disks appear to be quite halo-dominated (*e.g.* de Blok & McGaugh 1996, 1997; Swaters, Madore & Trewhella 2000), and should, in fact, violate the scale length–TF residual relation expected for maximal disks. However, to preserve the TF relation, either disks are negligible in all galaxies or the relation between halo/disk ratio and surface brightness must be fine-tuned.

The lack of correlation between scale length and  $\Delta V_{2.2}$  indicates that there is no feature in the rotation curve to distinguish putatively disk-dominated and halo-dominated portions of the rotation curve. This fine-tuning is related to the well-known “disk-halo conspiracy” noted by Bahcall & Casertano (1985): if disks are maximal, then disk and halo rotation curves must be of similar amplitude to maintain flat rotation curves (but see Casertano & van Gorkom 1991). The mystery in the end is why LSB and HSB disks lie on the same Tully-Fisher relation.

The best way to resolve the disk-halo degeneracy and its attendant problems, and to understand the origin of the Tully-Fisher relation, is to actually measure the degree of maximality of disks of galaxies over a range of velocity width and surface brightness. We are now attempting to make this measurement through observations of a number of barred galaxies. In this paper, we carry out this procedure for NGC 4123.

### 3. MODELING I. THE STELLAR MASS DISTRIBUTION

We wish to estimate the gravitational potential of the three-dimensional stellar mass distribution of the galaxy given a two-dimensional surface brightness distribution. There are three potential difficulties: spatial variations in  $M/L$  or extinction, deprojection to estimate the 3-D luminosity density from its projection into the 2-D plane of the sky, and conversion of luminosity density into mass density.

In fact, we do not need the full 3-D gravitational potential, but only its derivatives in the galaxy mid-plane – vertical gradients can be neglected. This is because the emission-line kinematic tracers we observe arise in the gas phase, which lies in a thin layer. (The H I disk can be warped and/or flaring at large radius, but these phenomena generally occur outside the optically luminous disk of the galaxy – see the review by Binney (1991).) This requirement considerably simplifies the task of deprojection.

As argued in Paper I, color and extinction variations are

mild in our  $I$  band image, and correcting for them would be quite model-dependent; we therefore neglect them here.

Projection is of course formally degenerate, and impossible to invert uniquely. One approach is to fit a 3-D parametric model to the data by projecting it into 2-D. Prolate Ferrers ellipsoids are the most convenient analytical forms with easily derived bar-like potentials, and several previous gas-dynamical studies of barred galaxies have used them to model bars. Duval & Athanassoula (1983) used a  $n = 0$  (uniform density) Ferrers bar in their study of NGC 5383, Regan *et al.* (1997) used a  $n = 1$  Ferrers bar to model NGC 1530, and we have used a  $n = 1$  Ferrers bar to model the Milky Way (Weiner & Sellwood 1999). Lindblad *et al.* (1996), on the other hand, used a photometric model less dependent on an analytical form to derive a potential for their gas-dynamical simulations, rectifying their  $J$ -band image of NGC 1365 to face-on and decomposing it into the first several even Fourier components.

A disadvantage of the analytical approach is evident from the  $I$ -band image of NGC 4123 presented in Paper I. The bar in this galaxy has a complex shape which does not lend itself to modeling by simple analytic expressions. It has two components, both of which are clearly non-ellipsoidal. The high surface brightness central component is distinctly rectangular, while the elongated component is also quite boxy and possibly broadens, if anything, towards the ends, where an ellipsoid would taper. We are therefore motivated to construct a model which is independent of analytic expressions for the luminosity density. Our approach is inspired by Quillen, Frogel & Gonzalez (1994), who estimated the potential of a face-on barred galaxy in a model-independent way by integrating over the actual light distribution. We wish to apply the same method to an inclined galaxy, which we must first deproject to face on.

### 3.1. Deprojection

Disk galaxies are relatively thin (*e.g.* van der Kruit & Searle 1982) and a simple stretch of our 2-D image should give us a reasonable approximation to a face-on view of the galaxy. As the galaxy has a finite scale height, which is probably not the same for all components, such a deprojection will introduce biases which we address in this section.

There are a number of foreground stars which must be removed before the rectification process. We masked out circular apertures around each star. NGC 4123 is very close to bisymmetric, especially in the bar region, so we replaced the missing data in the masked regions with the data from the corresponding regions after a  $180^\circ$  rotation. Since the galaxy is so bisymmetric, we chose to conserve computing resources by running our simulations on a half-plane and enforcing bisymmetry (see Section 5). We constructed a strictly bisymmetric image by rotating the image  $180^\circ$  and averaging the rotated and original images. We assume the inclination  $i = 45^\circ$ , derived from our kinematic data in Paper I, and simply stretch the galaxy image along the projected minor axis by the factor  $1/\cos i$  to produce a face-on image of surface brightness, while conserving total luminosity.

We selected NGC 4123 for this study in part because it does not have a large spheroidal bulge. In fact, the only spheroidal component present is a unresolved point-like

source at the very center of the galaxy (Paper I), having a luminosity  $1.8 \times 10^8 L_\odot$  in the  $I$ -band. We fit this source independently and remove it before deprojection.

The finite thicknesses of the disk and bar will introduce inaccuracies into our deprojection. The typical scale height of a disk is a few hundred parsecs, but the vertical extent of the bar may be up to 2–3 times greater. Bars in simulations develop pronounced “peanut” shapes (Combes & Sanders 1981; Raha *et al.* 1991) which have larger scale heights than the disk, and the box/peanut bulges seen in some edge-on galaxies are associated with bars (Kuijken & Merrifield 1995; Bureau & Freeman 1999). It is possible that the peanuts and boxes occur at the bar center, but that the bar is thinner further out along its length. Dettmar & Barteldrees (1990) showed that some edge-on galaxies with box and peanut bulges have an additional thin component which they suggest is a bar. NGC 4123 could be such an object, given the two-component structure of its bar (Paper I).

The bias introduced by rectification is significant only when a structure has a scale length  $s$  along the deprojected minor axis of the galaxy that is comparable to its vertical scale height  $z_0$ . At an inclination of  $i = 45^\circ$ , for example, erroneously rectifying a sphere with  $s = z_0$  would stretch it along the galaxy minor axis by a factor of 1.414, a 41% error in its linear extent. However, a spheroid with a modest 2:1 flattening ( $s = 2z_0$ ), once rectified, would be erroneously stretched by a factor of just 1.12, and for an object with 3:1 flattening the stretch is too large by just 5%. These factors are only marginally different for non-ellipsoidal cross-sections.

As noted above, the boxy structure of NGC 4123 inside  $\sim 15''$  radius could be thickened into a box- or peanut-type bulge. Our models may not be reliable in the very center for this reason, although the bulge is unlikely to be as thick as 1:1. Outside the central boxy structure, the bar is probably about as thin as the disk, and the rectification bias should be minimal. The elongated part of the bar has a projected scale length of  $s_{\text{proj}} \sim 16''$  on the plane of the sky, parallel to the galaxy minor axis (not the bar minor axis). The deprojected length  $s$  in the plane of the galaxy, parallel to the galaxy minor axis is greater,  $s \simeq 1.4s_{\text{proj}} = 2.4$  kpc. If the bar has a scale height typical of disk galaxies,  $z_0 \sim 400$  pc, as we have assumed, then the erroneous stretching induced by rectification is very small. Rectification stretches along the galaxy minor axis, not the bar minor axis, which works in our favor.

### 3.2. Calculating the potential

In order to calculate the gravitational field from this face-on image, we must make two additional assumptions: (1) some relation between light and mass and (2) a form for the vertical structure of the disk.

We follow usual practice by assuming that light is directly proportional to mass – that is, a constant  $M/L$  throughout the galaxy. This simplest possible assumption is generally reasonable in the inner parts of galaxies (see Kent 1986), as evidenced by weak color gradients and the success of maximum disk models with constant  $M/L$ . Barred galaxies generally have shallower abundance gradients than unbarred galaxies (*e.g.* Martin & Roy 1994; Zaritsky, Kennicutt & Huchra 1994), which suggests they are well mixed and any gradient in  $M/L$  must also be fairly

shallow.

We considered the effect of a radially varying  $M/L$  in Paper I. Even if the outer disk  $M/L$  at 15 kpc is just half that of the bar, the effect on the disk contribution to the rotation curve is just 5% at 15 kpc. Our modeling procedure is sensitive to the  $M/L$  inside the bar, and varying the disk  $M/L$  outside the bar makes little difference to the derived disk and halo masses.

The potential and accelerations in the midplane of a finite-thickness disk are weaker than those from a razor-thin disk. We assume a vertical distribution of the common form  $\rho(z) \propto \text{sech}^2(z/2z_0)$ , and a scale height of  $z_0 = 200$  pc – similar to that found in edge-on disk galaxies (van der Kruit & Searle 1982; de Grijs & van der Kruit 1996; de Grijs 1997) and slightly smaller than in the Milky Way, since NGC 4123 is smaller (Mihalas & Binney 1981). The scale height is effectively a smoothing length for the potential. With the  $z$ -distribution given, we calculate the potential and the accelerations at every point in the midplane, using a Fourier transform method to convolve a Green’s function with the surface density distribution (Hockney 1965).

The rectified  $I$ -band image from our CTIO 0.9-meter photometry (Paper I) taken in  $1.2''$  seeing has  $0.39''$  pixels; in order to keep the cell size and number of cells in the simulation grid reasonable, we binned it  $2 \times 2$  to make the pixel size  $0.78''$ , or 84.7 pc. We then used the FFT algorithm to generate the  $x$ - and  $y$ -acceleration components on a  $1024 \times 1024$  (87 kpc square) grid, although we use only a  $256 \times 512$  subsection of this grid for our simulations; the large grid ensures that forces from mass outside the subsection are calculated accurately. Since the FFT grid is larger than the field of the CTIO observations, we extrapolated the disk surface brightness profile. The extrapolation contains just 2% of the total disk luminosity and is consistent with the observed surface brightness profile from our wider-field Las Campanas photometry.

We tested the effect of changing the assumed scale height  $z_0$  by factors of up to 2. The effects on the velocity jump across the bar shock (see Figure 7) are fairly small; lowering the scale height makes little difference, while increasing the scale height to 800 pc weakens the predicted velocity jump slightly, which would require a slightly higher bar  $M/L$  to match the observations (see Section 7.4). The assumed scale height has little effect on our conclusions based on the strength of the velocity jump (since we conclude that the bar  $M/L$  is high). However, the smoothing due to the scale height does affect the models at  $R < 1$  kpc; the streaming motions at the inner Lindblad resonance (ILR) weaken with increasing scale height. Therefore the models are not robust inside the ILR (see Section 7).

The method also assumes that  $z_0$  is constant over the bar and disk. As argued above, only the inner  $10''$ – $15''$  of the bar can be substantially thicker than the disk, and the effect is small outside the innermost few grid cells; but inside  $\sim 10$  grid cells, the approximate size of the ILR, the potential could be affected by the uncertainty in scale height.

#### 4. MODELING II. ADDITIONAL MASS COMPONENTS

The total gravitational field must account for components of the mass distribution other than the stellar disk;

these include the nucleus, gas disk, and dark halo of NGC 4123.

We removed the central point-like source of  $1.8 \times 10^8 L_\odot$  from the image before the rectification described above. Its  $M/L$  is uncertain, since it is blue and an emission-line source, and is likely to have a young stellar population or even nonstellar luminosity, both suggesting a low  $M/L$ . Conversely, there could be a black hole at the center of NGC 4123, although upper limits on the black hole mass to bulge mass relation make it highly unlikely that a black hole in such a modest-sized galaxy could have a mass as high as  $10^8 M_\odot$  (Kormendy & Richstone 1995).

We modeled the nucleus/bulge as a spherical Gaussian distribution,  $\rho(r) \propto \exp(-r^2/r_c^2)$ , with a scale radius of 200 pc. We chose this scale radius to be softer than implied by the optical observations to keep the forces from varying too strongly over the innermost few grid cells, which would cause large numerical diffusion effects. The Gaussian profile drops off rapidly, so the softening affects the forces in only the innermost cells.

Since the  $M/L$  of the nucleus is uncertain, we ran sets of models with three different prescriptions for the  $M/L$ , setting  $\Upsilon_b/\Upsilon_d$ , the ratio of nucleus/bulge to disk  $M/L$ , equal to either 0, 0.5, or 1.0. The nuclear mass influences the gas flow by changing the strength or size of the inner Lindblad resonance (see Athanassoula 1992; Weiner & Sellwood 1999). While the different choices of nuclear mass do affect the flow in the inner few grid cells, the dynamical parameters disk  $M/L$  and bar pattern speed  $\Omega_p$  are robust against variations in nuclear mass, as discussed further in Section 7.

Our 21 cm observations of NGC 4123 (Paper I) revealed the presence of a large, extended H I disk, with a hole of lower surface density in its center. The total mass of atomic gas, including helium, is  $1.06 \times 10^{10} M_\odot$ . In Figure 8 of Paper I, we show the small contribution of the azimuthally averaged atomic gas to the rotation curve. In this paper, we add this axisymmetric contribution to that of the now non-axisymmetric stellar disk. We do not have a map of the molecular gas distribution; as discussed in Paper I, single-dish observations show that the contribution from molecular gas to the rotation curve is quite small, and we neglect it.

In Paper I, we found that the observed 1-D rotation curve of NGC 4123 can be fitted satisfactorily for a wide range of disk  $M/L$  by adding quite simple DM halo models. This property is true for many disk galaxies with extended 21 cm rotation curves and lies at the heart of the disk-halo degeneracy.

The DM halos used in the 2-D models of the velocity field considered here are identical to those determined by the fit to the 21 cm rotation curve for the corresponding axisymmetric  $M/L$  models in Paper I. As there, we study two sets of models having two different popular halo density profiles:

$$\rho_h(r) = \begin{cases} \rho_0 \frac{1}{1 + (r/r_c)^2}, & \text{pseudo-isothermal;} \\ \rho_s \frac{4r_s^3}{r(r + r_s)^2}. & \text{NFW-type.} \end{cases} \quad (1)$$

The density profile of the first set has the pseudo-isothermal form while that of the second set is an “NFW-type” power-

law profile (Navarro, Frenk, & White 1996) discussed more fully in Paper I.

For a given disk  $M/L$ , the best-fit pseudo-isothermal and NFW-type halo rotation curves both fit the axisymmetric rotation curve well. Since they are fitting the same data, the two halo contributions to the rotation curve are quite similar and substituting one halo profile for the other makes little difference to the gas flow pattern inside the bar region. In fact, the preferred values of the main parameters, disk  $M/L$  and  $\Omega_p$ , scarcely differ for the two possible halos (see Section 7).

We have assumed spherical halos. As noted in Paper I, a flattened halo with a slightly different density distribution could produce essentially the same rotation curve. Since our data are restricted to the midplane of the galaxy, they do not constrain the halo flattening, nor does the halo flattening affect the results. If the halo were non-axisymmetric, it could conceivably contribute to the observed non-circular streaming motions. However, to have a significant effect on our results, the halo would have to be both quite prolate inside the bar radius, where the non-circular motions are large, and axisymmetric further out so as to not disturb the apparently circular flow pattern in the outer disk – at which point it would be part of the bar, for all practical purposes.

## 5. MODELING III. FLUID DYNAMICAL MODELS

### 5.1. The model parameters

The disk  $M/L$  is the main parameter for the gravitational potential, and the nuclear mass and dark halo profile are subsidiary parameters. To run a simulation of the gas dynamics, we also need to know the bar pattern speed  $\Omega_p$ . For a given potential, the value of  $\Omega_p$  also determines the radius  $r_L$  of the Lagrange point  $L_1$  of the bar; a faster-rotating bar corresponds to a smaller Lagrange radius. A particle at the  $L_1$  point would rotate at the same angular speed as the bar, and so  $r_L$  is the corotation radius. Two models with the same  $\Omega_p$  and different  $M/L$  have similar, but not exactly equal, values of  $r_L$ , because the value of  $r_L$  depends somewhat on the shape of the potential.

We parametrized our models by  $M/L$  and  $\Omega_p$ , and calculated  $r_L/a$ , the ratio of the Lagrange radius to the bar semi-major axis, for each model. The ratio  $r_L/a$  is commonly used to characterize the bar pattern speed because it generalizes across galaxies of different rotation curve height and bar size. Bars with  $r_L/a \lesssim 1.5$  are generally considered to be “fast-rotating.” The elongated stellar orbits which are generally presumed to make up the bar are confined inside the well of the effective potential which extends to  $L_1$ , so  $r_L/a > 1.0$  is favored (*e.g.* Teuben & Sanders 1985; Binney & Tremaine 1987). See Elmegreen (1996) for a review of the issues surrounding pattern speeds and their determination in barred galaxies.

A “set” of models includes a full range of disk  $M/L$  and bar pattern speed  $\Omega_p$ . Each set is 88 models with all combinations of 8 values of disk  $M/L$  from {1.0, 1.5, 1.75, 2.0, 2.25, 2.5, 2.75, 3.0}, and 11 values of  $\Omega_p$  from {10, 12, 14, 16, 18, 19, 20, 21, 22, 23, 24} km s<sup>-1</sup> kpc<sup>-1</sup>.

In order to check the dependence of the models on the subsidiary parameters  $\Upsilon_b/\Upsilon_d$  and dark halo profile, we ran six sets of models covering the three choices of  $\Upsilon_b/\Upsilon_d$  {0.0, 0.5, 1.0} and the two halo profiles, isothermal and NFW-

type. We do not expect these subsidiary parameters to affect the models’ fit to the data nearly as strongly as the main parameters,  $M/L$  and  $\Omega_p$ . Conversely we do not expect to make a robust determination of  $\Upsilon_b/\Upsilon_d$  and halo profile from the models. In total, 528 models were run.

The models of the set with isothermal halos and  $\Upsilon_b/\Upsilon_d = 0.5$ , which contains the best-fitting model, are listed by  $M/L$  and  $\Omega_p$  in Table 1.

The  $M/L$  range covers from a  $M/L = 1.0$  disk, which is dominated by the dark halo at nearly all radii, to a super-maximal disk at the high end of  $M/L = 3.0$  (see Figure 8 of Paper I). The  $\Omega_p$  range covers from quite slow-rotating bars to super-fast bars with  $r_L/a < 1$ .

### 5.2. The fluid dynamical code

We used a two-dimensional grid-based gas dynamical code (kindly provided to us by E. Athanassoula) to simulate the gas flow in the models of NGC 4123. The FS2 code is a second-order, flux-splitting, Eulerian, grid code for an isothermal gas in an imposed gravitational potential, originally written by G. D. van Albada to model gas flow in barred galaxy potentials (van Albada 1985). Athanassoula (1992) used it to study gas flow patterns in a variety of model galaxy potentials. We have modified it to suit our approach, but the heart of the code remains the finite-difference scheme described by van Albada (1985).

By its nature, the code approximates the interstellar medium as an Eulerian fluid, smooth on scales of the grid cell size. Without some idealization it is hopeless to simulate the extremely complex dynamics of the multiphase ISM. Various methods including grid codes, particle hydrodynamics, and sticky-particle codes have been advocated (see Weiner & Sellwood 1999). Essentially, applying the Euler equations to the ISM simply asserts that the ISM has a pressure or sound speed defined in a coarse-grained sense, over scales greater than the code’s resolution.

The smoothed particle hydrodynamics (SPH) models of Englmaier & Gerhard (1997), who ran a simulation under the same conditions as used by Athanassoula (1992) with the FS2 Eulerian grid code, yielded very similar results. There are some small differences between the results of the grid and SPH codes, chiefly due to the different tradeoffs in resolution in Eulerian and Lagrangian schemes. However, the chief features, such as the strength of the shocks in the bar (see Section 7), are quite similar. This comparison reassures us that the simulation results are not dependent on the particular fluid-dynamical algorithm.

The code does not include the self-gravity of the gas, although the axisymmetrized rotation curve due to the atomic gas is included as part of our model for the potential, discussed above in Section 4. The gas self-gravity is negligible for this study, since the gas surface density is considerably lower than that of the stellar disk and of the halo. This is especially so in the bar region of NGC 4123, as can be seen from the rotation curve mass models in Figure 8 of Paper I. Since we compare the gas velocities to data only within the bar, the lack of gas self-gravity has little effect on the results.

We use a grid having 256 by 512 cells, each 84.7 pc square, and enforce a 180° rotation symmetry so that the grid is effectively 512 by 512 and bisymmetric. Tests show that the results are not dependent on the cell size. The barred potential rotates at a fixed pattern speed  $\Omega_p$ , and

$M/L_I$	$\Omega_p$	$r_L/a$	$\chi^2/N$	$\chi^2/N$
			raw errors	+ 8 km s <sup>-1</sup> dispersion
1.00	10.0	2.38	102.30	29.83
1.00	12.0	2.04	55.21	14.74
1.00	14.0	1.76	14.22	4.13
1.00	16.0	1.53	12.79	3.73
1.00	18.0	1.34	14.76	4.75
1.00	19.0	1.25	16.00	5.15
1.00	20.0	1.16	17.57	5.56
1.00	21.0	1.07	19.44	6.03
1.00	22.0	0.92	21.36	6.52
1.00	23.0	0.85	22.97	6.92
1.00	24.0	0.80	24.03	7.16
1.50	10.0	2.48	84.42	24.14
1.50	12.0	2.14	41.26	11.30
1.50	14.0	1.86	21.04	6.01
1.50	16.0	1.63	10.89	3.56
1.50	18.0	1.47	10.64	3.67
1.50	19.0	1.36	11.73	3.97
1.50	20.0	1.28	13.36	4.38
1.50	21.0	1.20	15.17	4.83
1.50	22.0	1.11	16.56	5.20
1.50	23.0	0.88	17.21	5.34
1.50	24.0	0.83	17.51	5.37
1.75	10.0	2.51	68.50	19.21
1.75	12.0	2.16	36.06	10.25
1.75	14.0	1.89	10.24	3.09
1.75	16.0	1.67	7.06	2.50
1.75	18.0	1.49	8.44	2.99
1.75	19.0	1.40	9.70	3.34
1.75	20.0	1.31	10.74	3.62
1.75	21.0	1.23	10.97	3.69
1.75	22.0	1.14	10.88	3.64
1.75	23.0	0.85	11.11	3.64
1.75	24.0	0.78	11.34	3.66
2.00	10.0	2.52	74.36	20.18
2.00	12.0	2.18	22.99	6.81
2.00	14.0	1.91	7.09	2.40
2.00	16.0	1.69	6.52	2.39
2.00	18.0	1.51	5.89	2.11
2.00	19.0	1.43	5.63	1.98
2.00	20.0	1.33	5.23	1.87
2.00	21.0	1.24	5.27	1.86
2.00	22.0	0.86	5.65	1.97
2.00	23.0	0.79	5.92	2.06
2.00	24.0	0.71	6.33	2.14

$M/L_I$	$\Omega_p$	$r_L/a$	$\chi^2/N$	$\chi^2/N$
			raw errors	+ 8 km s <sup>-1</sup> dispersion
2.25	10.0	2.53	70.29	19.56
2.25	12.0	2.18	22.89	7.54
2.25	14.0	1.93	12.56	4.67
2.25	16.0	1.70	7.41	2.64
2.25	18.0	1.53	6.27	2.23
2.25	19.0	1.46	4.81	1.84
2.25	20.0	1.35	3.54	1.40
2.25	21.0	1.26	3.78	1.42
2.25	22.0	0.85	4.22	1.55
2.25	23.0	0.77	4.59	1.64
2.25	24.0	0.68	4.87	1.67
2.50	10.0	2.54	86.60	26.20
2.50	12.0	2.20	89.74	25.09
2.50	14.0	1.96	40.68	12.66
2.50	16.0	1.73	20.93	7.16
2.50	18.0	1.55	6.53	2.32
2.50	19.0	1.48	8.50	3.03
2.50	20.0	1.39	5.36	2.10
2.50	21.0	1.31	5.11	1.87
2.50	22.0	0.87	5.07	1.82
2.50	23.0	0.80	4.33	1.60
2.50	24.0	0.71	4.36	1.55
2.75	10.0	2.54	129.66	36.64
2.75	12.0	2.22	138.08	38.19
2.75	14.0	1.99	62.56	19.22
2.75	16.0	1.77	36.94	11.44
2.75	18.0	1.58	17.23	6.12
2.75	19.0	1.51	7.88	2.86
2.75	20.0	1.46	9.83	3.22
2.75	21.0	1.36	7.68	2.82
2.75	22.0	1.28	6.93	2.48
2.75	23.0	0.85	6.13	2.21
2.75	24.0	0.78	5.46	1.93
3.00	10.0	2.57	196.67	52.13
3.00	12.0	2.25	186.90	51.66
3.00	14.0	2.04	80.47	23.89
3.00	16.0	1.84	48.29	14.96
3.00	18.0	1.63	37.61	11.50
3.00	19.0	1.55	22.39	7.45
3.00	20.0	1.49	14.74	5.48
3.00	21.0	1.43	10.49	3.39
3.00	22.0	1.34	11.43	3.97
3.00	23.0	1.27	10.22	3.31
3.00	24.0	0.85	7.84	2.75

TABLE 1  
SIMULATION PARAMETERS AND GOODNESS OF FIT

NOTE.— Simulations for the set of models with isothermal halos and  $\Upsilon_b/\Upsilon_d = 0.5$ , listed by their parameters  $M/L_I$  in Column 1 and  $\Omega_p$  in Column 2. Column 3 is the value of  $r_L/a$  implied by  $\Omega_p$ . Column 4 is the reduced  $\chi^2$  for the models' fit to the velocity data using purely statistical errors (see Section 7) and Column 5 is the reduced  $\chi^2$  when an additional 8 km s<sup>-1</sup> dispersion is added to the error budget.

the grid rotates with the bar. The  $x$ -axis of the grid is along the line of nodes of the galaxy disk. This puts the major axis of the bar at an angle of 53° to the  $x$ -axis. (It is desirable to avoid having the bar aligned with either the  $x$ - or  $y$ -axis of the grid.) The simulation timestep is variable, chosen automatically via a Courant condition, and is generally 0.1 – 0.2 Myr.

We take the sound speed of the gas to be 8 km s<sup>-1</sup> (similar to the Galactic value, *e.g.* Gunn, Knapp & Tremaine 1979), corresponding to a temperature of 10<sup>4</sup> K, a preferred temperature for the diffuse interstellar medium. Varying the sound speed within reasonable limits of several km s<sup>-1</sup> does not materially affect the derived gas flow. The strength and shape of the velocity jump across the primary shocks (see Figure 7) do not change much for simulations with sound speed  $c_s = 1$  to  $\sim 25$  km s<sup>-1</sup>. For  $c_s \gtrsim 50$  km s<sup>-1</sup>, the magnitude of the velocity jump decreases: the sound speed becomes comparable to the

streaming motions, and the shocks are no longer strong since the Mach number is not much greater than 1. However, such high sound speeds for the ISM are unrealistic; additionally, high sound speeds would require a more massive bar to produce the observed shock, and the bar we infer is already near-maximal (Section 7).

### 5.3. Initial conditions

We begin each simulation with an axisymmetric potential so that the gas starts on circular orbits. To achieve this, we redistribute the only non-axisymmetric part of the mass, the stellar disk and bar, by averaging it over azimuthal angle. We then cause linear growth of the bar by interpolating the gravitational field between the initial axisymmetric and the final observed barred shape. We allow 0.1 Gyr to reach the fully barred state, a time much longer than the timestep so that the flow adjusts steadily to the growth of the bar. The bar growth time is roughly

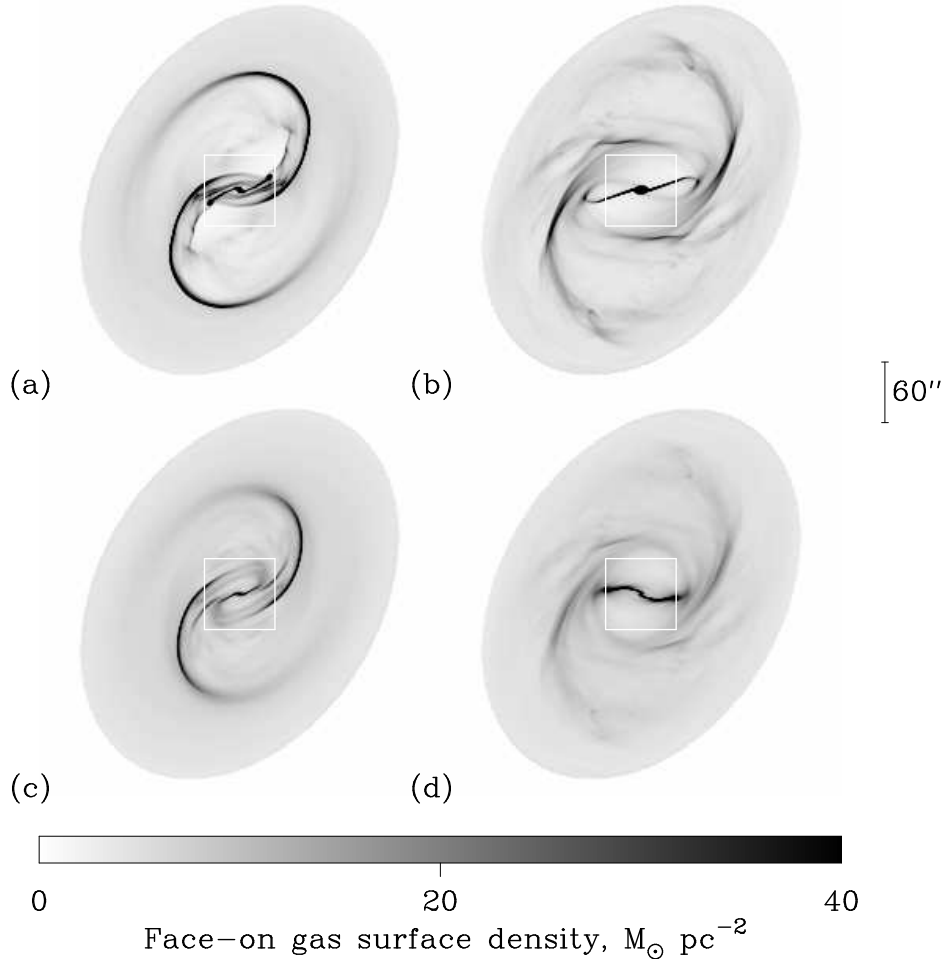


FIG. 1.— Projected view of the gas density field in four models

The gas density field in four representative simulations, at 0.2 Gyr simulation time, projected to the galaxy's orientation on the plane of the sky; north is up and west is to the right. The grayscale runs from 0 to  $40 \text{ M}_\odot \text{ pc}^{-2}$  in face-on gas surface density. The bar runs east-west, and the offset regions of high gas density along the bar are the loci of shocks. The white box indicates the bar region plotted in Figures 2 and 3. (a) Heavy disk, fast bar model with  $M/L = 2.25$ ,  $\Omega_p = 20 \text{ km s}^{-1} \text{ kpc}^{-1}$ . (b) Heavy disk, slow bar model with  $M/L = 2.25$ ,  $\Omega_p = 10 \text{ km s}^{-1} \text{ kpc}^{-1}$ . (c) Light disk, fast bar model with  $M/L = 1.0$ ,  $\Omega_p = 20 \text{ km s}^{-1} \text{ kpc}^{-1}$ . (d) Light disk, slow bar model with  $M/L = 1.0$ ,  $\Omega_p = 10 \text{ km s}^{-1} \text{ kpc}^{-1}$ .

one-third of an orbital period for material in the bar.

We set the initial gas surface density to be constant at  $10 \text{ M}_\odot \text{ pc}^{-2}$  inside a radius of 8 kpc; outside that radius it falls off exponentially with a scalelength of 13 kpc. These values were chosen by examining the H I data. (We did not use an initial density distribution with a central hole, because the H I hole is probably caused by the bar once it forms, and may be filled in by molecular gas.) Longer bar growth times and different initial density distributions have very little effect on the results.

The gas response can never reach a completely steady state, since the gas inside corotation will always lose angular momentum to the bar; however, after the bar growth time, the evolution of the gas flow pattern is quite slow.<sup>1</sup> We continue our simulations to 0.2 Gyr to allow the gas flow to settle after the bar has grown, and to 0.3 Gyr to

check that the flow has stabilized.

There are some small changes from 0.1 Gyr to 0.2 Gyr in the gas density and velocity fields in the bar region, as the gas response to the fully grown bar stabilizes. After 0.2 Gyr, gas continues to fall to the center, but there is little change in the velocity field in the bar region from 0.2 to 0.3 Gyr. We tested a bar growth time of 0.2 Gyr and found no significant difference after the gas response had settled.

In order to compare the simulations to the data, for each simulation we projected the gas velocity field at 0.2 Gyr into line-of-sight velocities, and scaled and rotated it to match the orientation of the observed Fabry-Perot velocity field of the bar region as shown in Paper I.

#### 5.4. The best fit model and variants

Figure 1 shows the gas density field viewed at 0.2 Gyr run-time in four representative simulations. Panel (a) has  $M/L = 2.25$  and  $\Omega_p = 20.0$ ,  $\Upsilon_b/\Upsilon_d = 0.5$ , and an isothermal halo. This is the best-fitting simulation discussed in Section 7. Panels (b-d) show variations on this model.

<sup>1</sup>Gas builds up in the center due to torque from the bar, which can be significant if the code is run for many rotation periods, *e.g.* several Gyr. We turned off gas recycling in the code: though it decreases mass buildup, it can provoke numerical instability (see Weiner & Sellwood 1999).

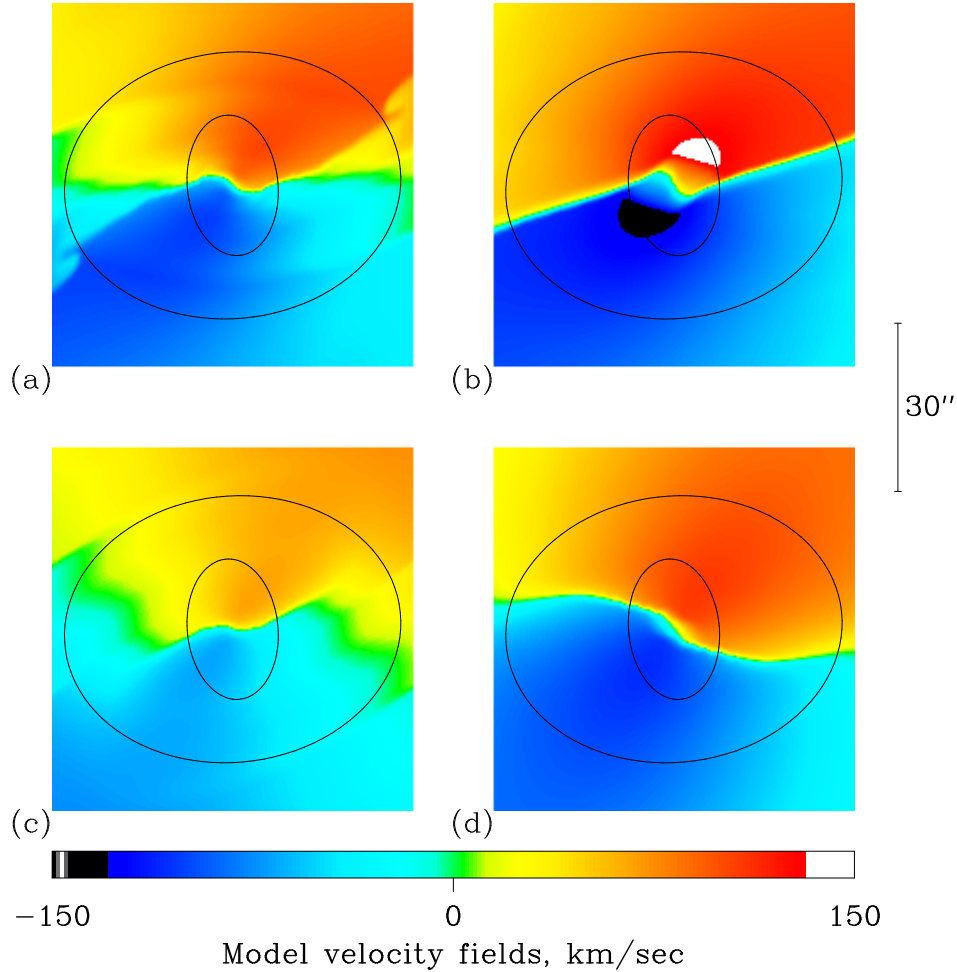


FIG. 2.— Four simulated gas velocity fields

Simulation velocity fields in the bar region (inset boxes in Figure 1), reprojected onto the plane of the sky to match the observations. North is up and west is to the right. The projected major axis of the galaxy is at  $57^\circ$  north of west. The color scale shows the line-of-sight velocity field. The bar runs approximately east-west and the shocks are the large velocity gradients perpendicular to the bar. The area between the ellipses is that used for comparison to the data in Section 7. Panels are as in Figure 1: (a) heavy disk,  $M/L = 2.25$ , fast bar; (b) heavy disk, slow bar; (c) light disk,  $M/L = 1.0$ , fast bar; (d) light disk, slow bar.

The density fields have been reprojected and rotated to match NGC 4123's orientation on the plane of the sky, for purposes of comparison. Shocks in the bar, visible as regions of high gas density, are associated with jumps in the model gas velocity field. There are multiple regions of high gas density in the bar, which correspond to a very strong primary shock and some smaller secondary shocks. The straight features of high gas density traceable from the center are the locations of the primary shocks, and correspond to the dust lanes visible in the colormap, Figure 2 of Paper I. The natural explanation for the cause of the shock is the elongation of the streamlines along the bar (see the discussion of Prendergast 1983). Gas falling down along the bar potential reaches high velocities, and as the gas climbs away from the center, up the potential, it decelerates. Eventually a pile-up occurs and the shock is formed. The strength and location of the gradient and shock are strongly influenced by the ellipticity and rotation rate of the potential.

A massive bar causes a strong spiral pattern in the gas disk outside the bar region, as can be seen in Figure 1.

The spiral response is enhanced by the spiral structure and mild ellipticity of the stellar disk outside the bar, discussed in Paper I; our simulation method causes the outer disk structure to rotate at the same angular speed as the bar. An additional simulation of a model in which we forced the disk outside the bar to be axisymmetric still generated a weaker spiral arm pattern.

The spiral pattern continues to evolve from 0.2 Gyr to 0.3 Gyr, propagating outward and winding up to tighter pitch angles. We ran another test simulation for a long time (over 1 Gyr) and determined that the spiral continues to wind slowly. The spiral pattern is expected to evolve on a much longer timescale than the gas flow in the bar since the orbital timescale (the rotation period) is considerably longer at the larger radii where the spiral pattern occurs, and forcing from the bar is greatly reduced outside the bar radius. The steadiness of the gas flow pattern inside the bar allows us to compare a snapshot of the simulation to the observed velocity field inside the bar radius. The evolution of the spiral pattern renders a snapshot comparison to observations outside the bar radius unreliable;



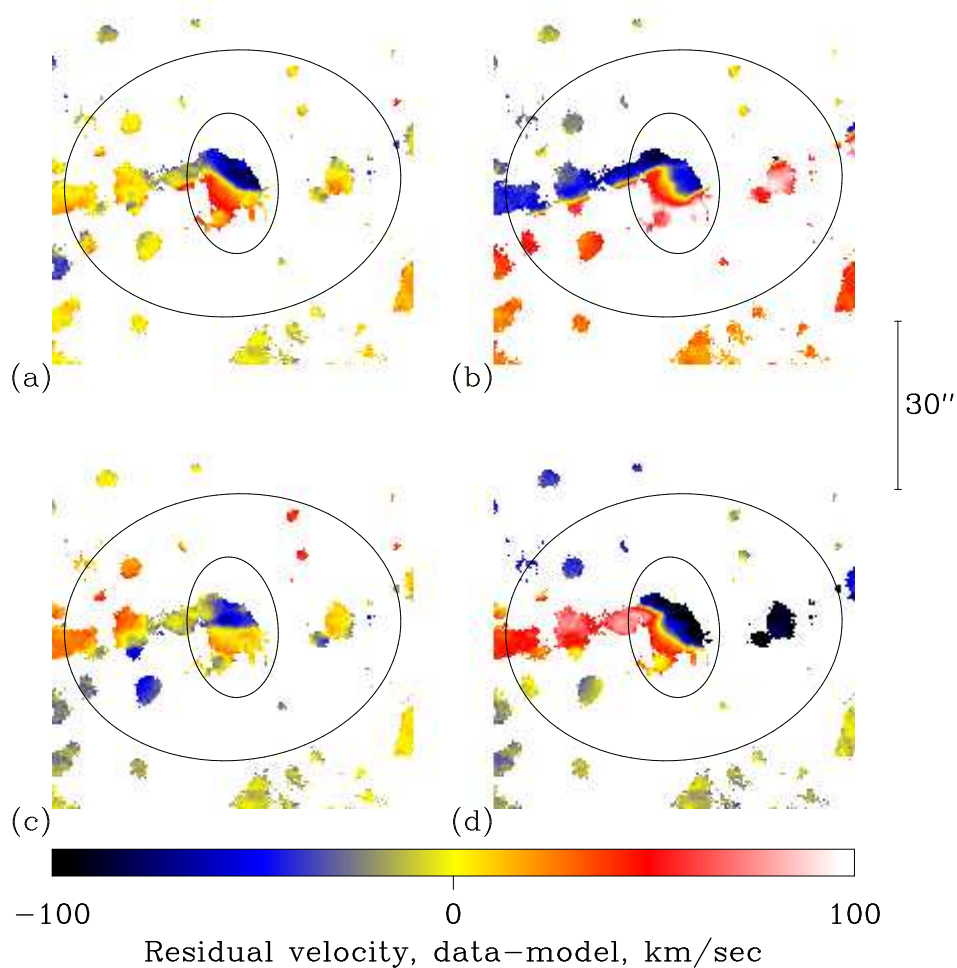


FIG. 3.— Residual velocity fields

Residual velocity fields in the bar region (inset boxes in Figure 1), for four representative models. The residuals are the Fabry-Perot velocity field from Paper I, minus each of the four models shown in Figure 2. The orientation is as in Figure 2. The area between the ellipses is that used for comparison to the data in Section 7. All models have large residuals inside the inner ellipse ( $8''$  radius), where both data and models are unreliable due to limited resolution; see Section 7.1. Outside that radius, model (a) has significantly smaller residuals than the others. Panels are as in Figure 1: (a) heavy disk,  $M/L = 2.25$ , fast bar; (b) heavy disk, slow bar; (c) light disk,  $M/L = 1.0$ , fast bar; (d) light disk, slow bar.

fortunately, most non-circular motions are inside the bar radius, as discussed in Paper I.

#### 6. FEATURES OF THE SIMULATED VELOCITY FIELDS

The models consist of two-dimensional velocity fields over the two-dimensional  $(M/L, \Omega_p)$  parameter space with the two subsidiary dimensions of  $\Upsilon_b/\Upsilon_d$  and halo type. It is impossible to show anything more than a small fraction of the models without overwhelming the reader. We present four representative models in Figures 1, 2, and 3 and discuss some of their features. These models are drawn from the set with  $\Upsilon_b/\Upsilon_d = 0.5$  and isothermal halos, and represent both low and high mass disks and low and high pattern speeds. In Section 7.4, we also discuss the systematic changes of the model velocity fields with  $M/L$  and  $\Omega_p$ , plotting 1-D subsets of the models against the observations.

##### 6.1. Low versus high mass disks

Panels (a) and (c) of Figure 2 show the effect of varying the disk mass. These are two simulated velocity fields

which differ only in disk  $M/L$ . The field in panel (a) is for an approximately maximum disk ( $M/L = 2.25$ ), while the field in panel (c) is for a low-mass disk, with  $M/L = 1.0$ , or about 40% of the maximum disk. Both are for fast-rotating bars, with  $\Omega_p = 20$ , corresponding to  $r_L/a = 1.16$  and  $1.35$ , respectively. The velocity fields have been reprojected into the plane of the sky, and rotated to match the observations shown in Paper I. The projected major axis of the galaxy is at  $57^\circ$  north of west, while the major axis of the bar runs nearly east-west.

The shocks in the bar are the roughly horizontal (east-west) isovels in the inner  $60''$  of each simulation. Across these isovels, perpendicular to the bar, there is a velocity gradient, particularly large in panels (a) and (b). The low  $M/L$  simulations produce less of a shock in the bar than the high  $M/L$  simulations, as can be seen by examining the bar region of the simulated velocity fields in panels (c) and (a). Strongly non-axisymmetric motion in the low mass disk (c) is restricted to the inner  $15''$  radius ( $\sim 1.6$  kpc), and the magnitude of the velocity jump across the shock is not large except very close to the bar center. By

contrast, the heavy disk produces offset shocks parallel to the bar which extend to two or three times farther out, and have larger velocity jumps.

The residual velocity fields in panels (a) and (c) of Figure 3 show the importance of the change in shock strength with  $M/L$ . The fast bar, high  $M/L$  simulation in panel (a) matches the observed velocities fairly well outside the ILR. By contrast, the fast bar, low  $M/L$  simulation in panel (c) produces large systematic residuals up to  $50 \text{ km s}^{-1}$ , north and south of the bar, because the velocity jump across the shock is not large enough, as discussed further in Section 7.4. Inside the ILR, all models show large residuals, which are not meaningful (see Section 7.1); both data and models are affected by limited resolution, and the structure of the ILR is more sensitive to  $\Upsilon_b/\Upsilon_d$  than global  $M/L$ .

As discussed above in Section 5, both simulations produce a spiral pattern driven by the bar; the pattern is stronger in the high  $M/L$  simulation, as is to be expected. The curving shocks to the southeast and northwest are along the spiral arms. The spiral arms in the high  $M/L$  velocity field of panel (a) are in approximately the same position as the actual spiral arms observed in NGC 4123 just outside the bar. These spiral arms are also visible in the Fabry-Perot  $\text{H}\alpha$  velocity field of NGC 4123, Figure 4 of Paper I, as chains of large bright  $\text{H II}$  regions. However, the spiral arms are not a particularly good argument for or against any model because the spiral pattern evolves over time, as mentioned in Section 5. Furthermore, the strength of the spiral arm density contrast and the associated shock are quite strong early in their evolution, stronger than is observed; and the observed spiral pattern actually appears to have a slower pattern speed than the bar, as discussed in Paper I. These factors suggest that the observed spiral pattern in the outer disk is decoupled or at best in resonance with the bar, rather than directly driven by it (see Sellwood & Sparke 1988).

### 6.2. Fast versus slow bars

Panels (a) and (b) of Figure 2 show the effect of varying the bar rotation speed while holding the  $M/L$  fixed at 2.25, close to the maximum disk value. Panel (a) is for a fast-rotating bar, with  $\Omega_p = 20 \text{ km s}^{-1} \text{ kpc}^{-1}$  and  $r_L/a = 1.35$ , while panel (b) is for a slow bar, with  $\Omega_p = 10$  and  $r_L/a = 2.53$ .

The simulation with a fast-rotating bar produces offset shocks which lie almost parallel to the bar approximately at the location of the observed shocks and their associated dust lanes. The slow-rotating bar also produces shocks, but the magnitude and extent of the shocks are larger, and the location of the shocks shifts somewhat. Both effects occur because the gas overtakes the slow-rotating bar at a much higher relative speed; see Section 7.4 below.

Panels (a) and (b) of Figure 3 show the velocity residuals for these models. While the fast bar, high  $M/L$  model does fairly well (outside the ILR), the slow bar model in panel (b) has very large residuals. The velocity jump across the shock is too large and too sharp, causing substantial residuals of  $\gtrsim 50 \text{ km s}^{-1}$ ; see also Section 7.4.

Finally, panel (d) of Figure 2 shows the velocity field for a light disk,  $M/L = 1.0$ , and slow bar,  $\Omega_p = 10$  ( $r_L/a = 2.38$ ). There is a fairly strong shock in this model,

despite the low  $M/L$ , because the gas streams through the bar at higher relative speed. However, the shock is displaced very far upstream (in the direction of galactic rotation) compared with the other models; it is so far from the bar major axis that it is practically out of the bar, in strong disagreement with the observed location. This disagreement is reflected in the very large residuals,  $\sim 100 \text{ km s}^{-1}$ , seen in Figure 3(d).

## 7. COMPARISON OF SIMULATED VELOCITY FIELDS TO DATA

We have simulated gas velocity fields for six sets of 88 combinations of mass-to-light ratio and pattern speed. We reproject and rotate the velocity field of each simulation into the orientation of the galaxy on the plane of the sky, and estimate how well it resembles our observed velocity field. As our goodness-of-fit tests yield remarkably tight constraints on our main parameters,  $M/L$  and  $\Omega_p$ , we also offer simple physical explanations for the systematic changes, which we illustrate by taking one-dimensional cuts through the velocity fields for several ranges of models.

### 7.1. The region used for the comparison

For a meaningful comparison of models to data, it is necessary to use only regions where models and data are primarily sensitive to the parameters being varied and not to other systematic effects. We compare the models and data only in the area between the two ellipses on the sky indicated in Figures 2 and 3, and in Figure 4 of Paper I. The outer has diameters  $60''$  by  $48''$ , the inner has diameters  $24''$  by  $16''$ . The outer ellipse is chosen to include nearly all the emission within the bar, but exclude the large  $\text{H II}$  regions at the end of the bar, near the beginning of the spiral arms. The inner ellipse is chosen to exclude the knot of emission at the very center of the bar.

We chose this region of the data for several reasons. The region of most interest is inside the bar radius, where the non-axisymmetric motions are strong. Outside the bar radius, there are plenty of velocities with small errors derived from strong  $\text{H}\alpha$  emission, but including them in the comparison would place a large statistical weight on regions where the bar-induced motions are weak and therefore carry little useful information. Furthermore, the spiral arm patterns, which are the main source of non-circular motions outside the bar, evolve over time (Section 5). While the galaxy itself does have spiral arms and associated velocity perturbations, comparing them to the spirals in simulations which have not settled would be misguided.

We also exclude data at the very center of the galaxy. The velocity gradients are extremely high in this region, and are probably unresolved in our data. Also, there are several reasons why our models are most unreliable in this region: our model for the nucleus is probably too soft, deprojection errors from the thicker part of the bar are likely to be the most significant there, our assumption of uniform  $z$ -thickness is likely to be violated, and the resolution of the gas-dynamical code is also worst in the center, in the sense of having relatively few grid cells across the scale of a streamline. None of these problems are troublesome outside  $R \sim 10''$ , but together they force us to exclude data within that radius from the comparison.

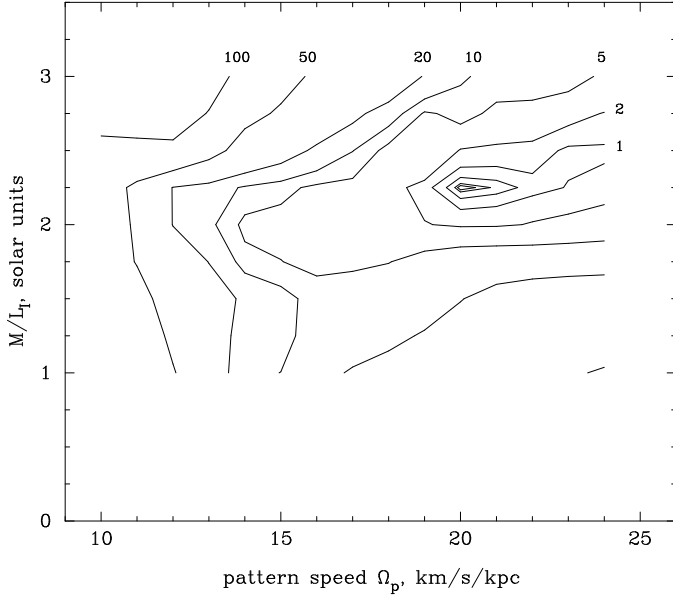


FIG. 4.— Quality of models' fit to the velocity data. I  
A contour plot of  $\chi^2/N$  over the  $\Omega_p - M/L$  plane for the 88 models in the set with isothermal halos and  $\Upsilon_b/\Upsilon_d = 0.5$ , calculated using strictly statistical velocity errors. The contours are  $\Delta(\chi^2/N) = 0.1, 0.2, 0.5, 1, 2, 5, 10, 20, 50, 100$ , with  $N = 471$ , surrounding the minimum:  $\chi^2/N = 3.54$ , at  $M/L = 2.25$  and  $\Omega_p = 20$ .

The distribution of H $\alpha$  emission, and hence velocity data, is rather sparse within our comparison region. However, there is still a substantial amount of data. In particular, there are emission regions within and on either side of the bar, which allow us to measure the strength and the location of the main bar shock. As seen in Figure 3, all of the emission regions within the bar (but outside the ILR) provide power to discriminate between models.

### 7.2. Overall comparison and likelihood

Within the comparison area – including the bar, but excluding the central region and the disk outside the bar – we can simply use our observed velocities and their associated errors to compute the chi-squared statistic as a measure of how well the models fit the data. Since our velocity data are oversampled, on  $0.36''$  pixels but with  $1.3''$  seeing, we binned down the velocity with a  $2 \times 2$  bin, to provide  $0.72''$  sampling as a compromise between preserving resolution in the velocity field and attaining statistical independence for adjacent pixels. This sampling approximately matches the models, which we do not need to smooth to equalize their resolution. Other choices, such as no binning, or a  $3 \times 3$  bin (which undersamples the seeing) produce different values of reduced  $\chi^2$ , but the relative quality of the models is similar to that presented below. Overlarge binning makes  $\chi^2$  artificially low, since it smooths both data and model heavily.

After the  $2 \times 2$  binning, we have  $N = 471$  velocity measurements within the region of interest, with errors ranging from  $2.5$  to  $12 \text{ km s}^{-1}$ ; the median error is  $7.4 \text{ km s}^{-1}$ . These errors are strictly statistical errors from the Voigt profile fitting to the Fabry-Perot data (see Paper I). For each simulation, we calculated  $\chi^2$  of the model, after computing the best-fit galaxy systemic velocity and subtract-

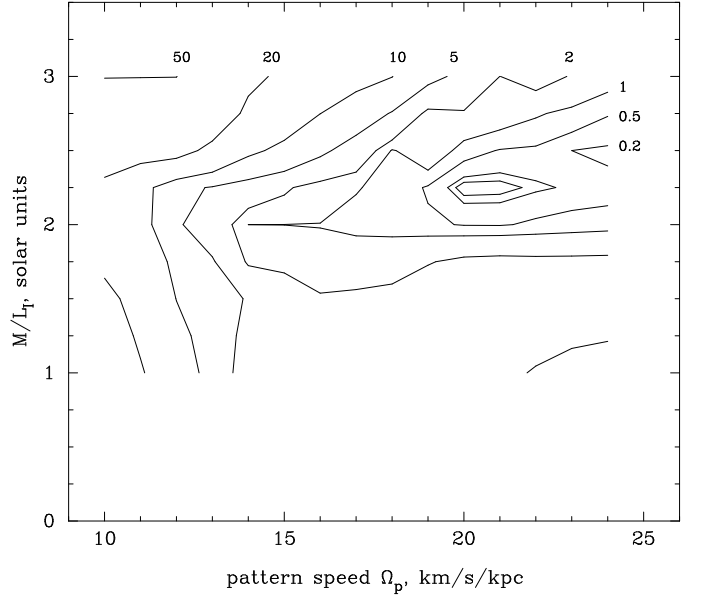


FIG. 5.— Quality of models' fit to the velocity data. II  
A contour plot of  $\chi^2/N$  over the  $\Omega_p - M/L$  plane for the 88 models in the set with isothermal halos and  $\Upsilon_b/\Upsilon_d = 0.5$ , calculated using the statistical velocity errors and an additional  $8 \text{ km s}^{-1}$  dispersion. The contours are  $\Delta(\chi^2/N) = 0.1, 0.2, 0.5, 1, 2, 5, 10, 20, 50$ , with  $N = 471$ , surrounding the minimum:  $\chi^2/N = 1.40$ , at  $M/L = 2.25$  and  $\Omega_p = 20$ .

ing it from the observations. For the set with isothermal halos and  $\Upsilon_b/\Upsilon_d = 0.5$ , the reduced value  $\chi^2/N$  is tabulated with the models in Column 4 of Table 1. Examining the results in Table 1 and Figure 4, it is clear that heavy-disk, fast-bar models with  $M/L \geq 2.0$  and  $\Omega_p \geq 18$  are the best match to the data. The best fit is for  $M/L = 2.25$  and  $\Omega_p = 20$ . Light disks and slow bars yield miserable fits.

The best models are not perfect fits to the data, in the sense of attaining  $\chi^2/N \leq 1.0$ . Given the number of idealizations inherent in the modeling procedure, this is not surprising, and we cannot expect the models to reproduce every feature of the data.

Another issue is that the purely statistical errors on the velocity data are not completely realistic. Many pixels in bright H II regions have errors much less than  $8 \text{ km s}^{-1}$  which are highly weighted in the computation of  $\chi^2$ , probably excessively so. A given line of sight is likely pass through one to a few H II regions, each of which may have a velocity different from the bulk matter-weighted velocity; our measurement is emission-weighted, and biased toward dense regions, since H $\alpha$  emission measure is proportional to  $n_e^2 l$ . Hence our H $\alpha$  measurements may not sample the mean velocity field fairly, and the velocity uncertainties should be adjusted for the rms offset of an individual H II region from the mean.

In order to get a sense of the importance of this effect, we added an additional *ad hoc* dispersion component of  $8 \text{ km s}^{-1}$  in quadrature to the initial error estimate. This is equal to the gas sound speed we assumed in our models and a reasonable estimate for the velocity dispersion among H II regions. The effect is to reduce the weight of very-low-error velocity measurements somewhat, giving

the “better” values of  $\chi^2/N$  tabulated in Column 5 of Table 1. As a trade-off, some discriminatory power is lost – the difference in goodness-of-fit between models is somewhat lessened. However, the conclusions are unchanged; light disks and slow bars are still grossly worse fits to the data. In practice, the purely statistical velocity errors are certainly underestimates, since no systematic effects have been budgeted for, while the boosted error bars probably make the models look too good. The two values of  $\chi^2/N$  in Columns 4 and 5 of Table 1 then bracket the amount of confidence one should have in a given model.

Figures 4 and 5 show contour plots of  $\chi^2/N$  distributed on the  $\Omega_p - M/L$  plane. Figure 4 shows the values of  $\chi^2/N$  calculated using the strictly statistical velocity error bars, and Figure 5 shows  $\chi^2/N$  calculated with the additional  $8 \text{ km s}^{-1}$  dispersion added to the error budget. These figures show graphically – in both senses of the word – that only heavy-disk, fast-bar models work. Low  $M/L$  disks and slow bars are ruled out.

The models which fit the data reasonably well range from  $M/L = 2.0$  to  $2.5$ , and from  $\Omega_p = 18$  to  $24 \text{ km s}^{-1} \text{ kpc}^{-1}$  ( $r_L/a = 1.5$  to  $0.8$ ). The disk of NGC 4123 is between 80% and 100% of the maximum disk mass and the bar is fast-rotating.

If instead of adding an additional  $8 \text{ km s}^{-1}$  dispersion error component, we add  $10.8 \text{ km s}^{-1}$  dispersion, then the best model, with  $M/L = 2.25$  and  $\Omega_p = 20$ , has  $\chi^2/N = 1.00$ . We can then use the values of  $\chi^2$  obtained using this additional  $10.8 \text{ km s}^{-1}$  error to determine confidence limits. Formally, all models but the best few are ruled out. At the 99.99% confidence level, the models allowed must have  $\Delta\chi^2 < 20$ , or  $\Delta(\chi^2/N) < 0.04$ . The only models allowed are the two with  $M/L = 2.25$  and  $\Omega_p = 20, 21$ . Even if we attempt to compensate for the correlation in measurements introduced by the seeing, assuming the number of independent measurements is only one-third of  $N = 471$ , the only models allowed at 99.99% confidence are those with  $M/L = 2.25$  and  $\Omega_p = 20$  to  $24$ , and the model with  $M/L = 2.5$  and  $\Omega_p = 23$ .

In practice, these restrictive limits are partly due to the assumption that all the sources of error are Gaussian. The level of statistical significance is nonetheless impressive – models in Figures 4 and 5 with somewhat worse values of  $\chi^2/N$  are in fact much poorer matches to the data.

### 7.3. Results for other model sets

We show in Figure 6 the results for all six sets of models, again plotting  $\Delta(\chi^2/N)$  over the  $\Omega_p - M/L$  plane for each set. Although the variation of  $\chi^2/N$  for different sets differs slightly in the details, the primary result is the same. The best model always has  $M/L$  of 2 or 2.25 and  $\Omega_p$  in the range  $18 - 23 \text{ km s}^{-1} \text{ kpc}^{-1}$ . Models with  $M/L < 2$  or  $\Omega_p < 18$  are always significantly worse. Figure 6 shows that the subsidiary parameters of halo shape and  $\Upsilon_b/\Upsilon_d$  have little effect on the distribution of  $\Delta(\chi^2/N)$ .

We also computed the results for all sets of models when an additional  $8 \text{ km s}^{-1}$  dispersion is added to the statistical errors on the observed velocities, as described above. This procedure weights the observed velocities slightly differently, and in down-weighting velocity measurements with extremely small errors, is probably a more realistic basis for choosing the best-fit model. When we compute

values of  $\chi^2/N$  with the added  $8 \text{ km s}^{-1}$  dispersion, the best model, with  $M/L = 2.25$ ,  $\Omega_p = 20$ ,  $\Upsilon_b/\Upsilon_d = 0.5$ , and isothermal halo, remains the best; the model with the same parameters but  $\Upsilon_b/\Upsilon_d = 0$  is almost as good. For each set of  $\Upsilon_b/\Upsilon_d$  and halo type, the best model always has  $M/L = 2.25$  and  $\Omega_p$  in the range  $20 - 23 \text{ km s}^{-1} \text{ kpc}^{-1}$ . Models with  $M/L < 2$  and  $\Omega_p < 18$  are always ruled out at the 99.99% confidence level.

No matter how we model the nucleus and the halo, or treat the errors on the observed velocities, Figure 6 shows that the best models are always in the same region of  $M/L$  and  $\Omega_p$ , requiring a heavy disk and fast bar. The six sets of models have best values of  $\chi^2/N$  which differ somewhat: there is some preference for a low  $M/L$  for the nucleus, which is plausible since it is blue and an emission-line source. There is not a strong discrimination between NFW and isothermal halo profiles. Overall, the best value for disk  $M/L_I$  is 2.25, and  $M/L_I = 2.0$  is a strong lower limit.

Since we have compared the models to velocity data only within the bar radius, technically we require only that  $M/L$  must be high within the bar radius. However, in Paper I we showed that an  $M/L$  which begins to decline outside the bar radius does not cause a significant decrease in the disk contribution to the rotation curve. Therefore, the high  $M/L$  indicates that the disk contribution is at or near maximum.

### 7.4. A slit cut through the data and models

The previous comparisons of our models with 2-D data indicate very tight constraints on our two main parameters. In order to gain a physical understanding of these constraints, we examine a subset of the data in more detail. As we emphasized in Paper I, the strongest signatures of the non-axisymmetric motions caused by the bar are the offset shocks along the bar, which are also the locations of the dust lanes. We extract a slice nearly perpendicular to the bar from the Fabry-Perot data in order to show the velocity jump in the shock, which we compare with the corresponding data from the models. We make this comparison for two subsets of the 2-parameter  $M/L - \Omega_p$  space which include our best-fitting model, for which  $M/L = 2.25$ ,  $\Omega_p = 20$ .

The position of our pseudo-slit through the Fabry-Perot data is indicated by the vertical line in Figure 4 of Paper I. It is at  $17''$  (2 kpc distance in the disk) east of the galaxy center, runs north-south, nearly perpendicular to the bar, and is 2 pixels, or  $0.72''$ , wide. We selected it to pass through several regions of H $\alpha$  emission, including one which straddles the velocity jump associated with the shock, and two regions of H $\alpha$  emission on either side of the shock. The spatial resolution of the data and models shown here are similar – about  $1.4''$  for both.

The velocity data are the points with error bars plotted in Figures 7 and 8, while the predictions from sets of models are drawn as smooth curves. The  $x$ -axis is distance from the bar major axis in arcsec, in the direction of galaxy rotation, so that gas overtakes the bar moving from left to right on this plot. The  $y$ -axis is projected line-of-sight velocity. The strong gradient in the central part of the data is a combination of the changing projection of the gas streamlines, and the shock at the leading edge of the bar. The gradient is clearly spatially resolved. The two

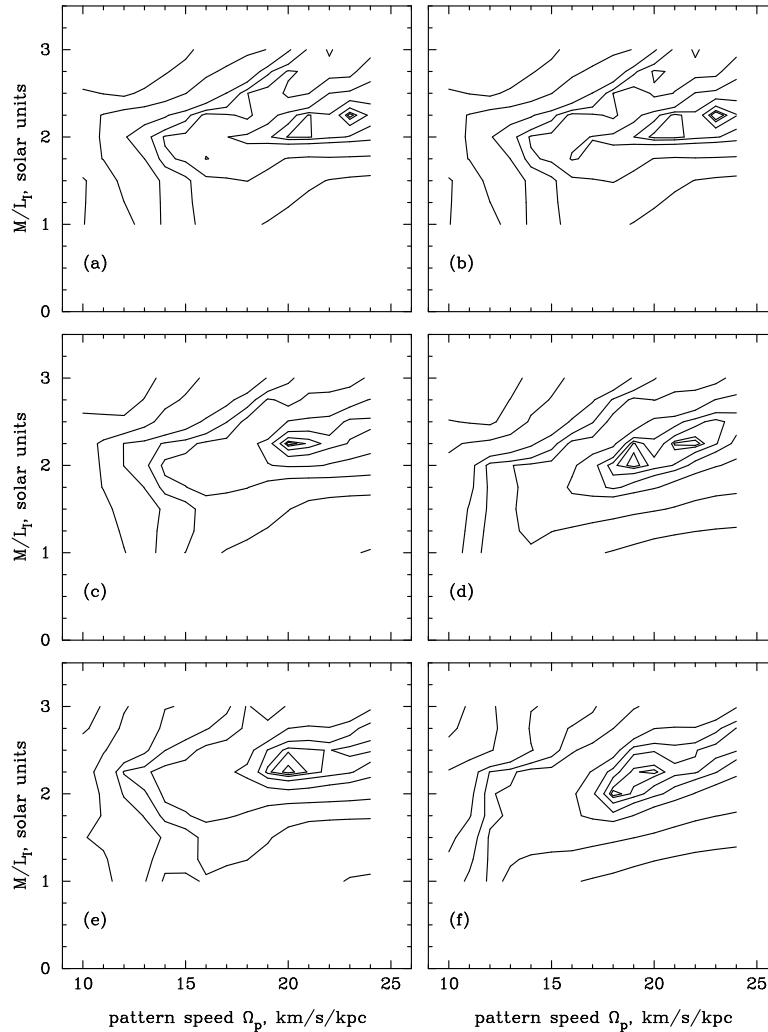


FIG. 6.— Quality of models' fit to the velocity data, for all models

The value of  $\chi^2/N$  is shown over the  $\Omega_p - M/L$  plane, for all six sets of models, calculated using strictly statistical velocity errors. Each set contains 88 models. The left column is for isothermal halos, the right for pseudo-NFW halos. The top row has  $\Upsilon_b/\Upsilon_d = 1$ , the middle row  $\Upsilon_b/\Upsilon_d = 0.5$ , the bottom row  $\Upsilon_b/\Upsilon_d = 0.0$ . The contours are  $\Delta(\chi^2/N) = 0.1, 0.2, 0.5, 1, 2, 5, 10, 20, 50, 100$ .

(a) Isothermal halos,  $\Upsilon_b/\Upsilon_d = 1.0$ , best  $\chi^2/N = 4.90$ . (b) NFW halos,  $\Upsilon_b/\Upsilon_d = 1.0$ , best  $\chi^2/N = 5.02$ . (c) Isothermal halos,  $\Upsilon_b/\Upsilon_d = 0.5$ , best  $\chi^2/N = 3.54$ . (d) NFW halos,  $\Upsilon_b/\Upsilon_d = 0.5$ , best  $\chi^2/N = 4.08$ . (e) Isothermal halos,  $\Upsilon_b/\Upsilon_d = 0.0$ , best  $\chi^2/N = 3.74$ . (f) NFW halos,  $\Upsilon_b/\Upsilon_d = 0.0$ , best  $\chi^2/N = 3.94$ .

H II regions away from the shock do not have significant internal velocity gradients.

The change in velocity from one side of the bar to the other is  $140 \text{ km s}^{-1}$  in line-of-sight velocity (uncorrected for inclination), a substantial fraction of the velocity width of the galaxy. This gradient arises from the changing projection of the non-circular streamlines and the shock in the bar (see the velocity field in Paper I). The shock is caused by elongation of the streamlines along the bar, so its strength is closely dependent on the bar mass, which controls the ellipticity of the potential.

#### 7.4.1. Varying the disk mass

In Figure 7, we keep  $\Omega_p$  fixed at 20 and plot four models with  $M/L = 1.0, 1.75, 2.25$ , and  $3.0$ . At  $M/L = 1.0$ , the simulation predicts a rather small velocity change, less than half that observed, but the velocity change increases and becomes steeper as  $M/L$  rises. Furthermore, there is a systematic shift in the position of the strong shock, where

the gradient is steepest; the much smaller velocity wiggles are due to secondary shocks. Of these four models, only that with  $M/L = 2.25$  shows a shock of about the right strength at the location of the observed velocity jump.

The constraint on  $M/L$  is strikingly tight. Non-axisymmetric forces become weaker as  $M/L$  decreases, as the influence of the bar declines and that of the round halo grows. Models with  $M/L < 2.0$  cannot produce a strong enough shock, even at 2 kpc from the galaxy center. The presence of shocks with a large velocity jump along the length of the bar requires that the streamlines be quite elliptical, which requires a massive bar. If the dark matter is dominant in the inner disk, the potential is rounder and cannot produce the shocks.

#### 7.4.2. Varying the pattern speed

In Figure 8, we keep  $M/L$  fixed at 2.25 and plot models of varying  $\Omega_p$ . The models plotted have  $\Omega_p = 10, 14, 20$ , and  $24 \text{ km s}^{-1} \text{ kpc}^{-1}$ , corresponding to  $r_L/a = 2.53, 1.93$ ,

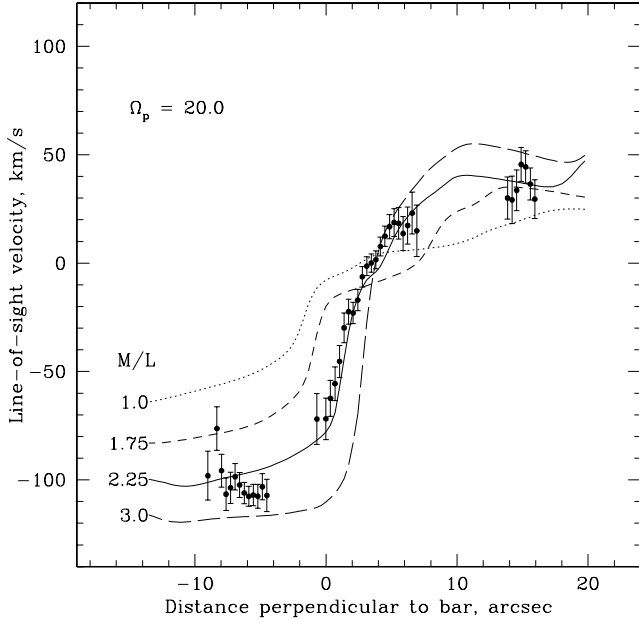


FIG. 7.— A cut through the velocity data and models of varying  $M/L$ . The Fabry-Perot velocity data (points) and associated errors from a pseudo-slit cut through the data, nearly perpendicular to the bar. The x-axis is distance from the bar in arcsec, The y-axis is line-of-sight velocity. The lines are the velocity fields of models; all have  $\Omega_p = 20$ . The  $M/L$  values and line styles are 1.0 (dotted), 1.75 (short dash), 2.25 (solid), and 3.0 (long dash).

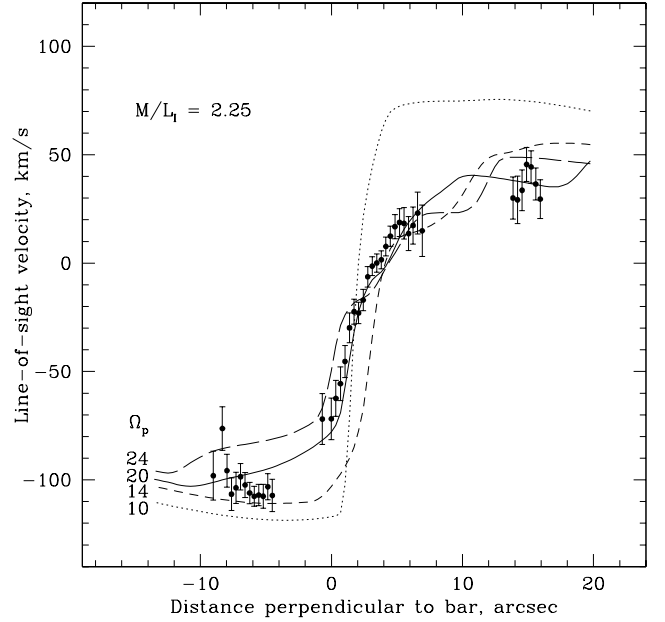


FIG. 8.— A cut through the velocity data and models of varying  $r_L/a$ . The Fabry-Perot velocity data (points) and associated errors from a cut through the data, nearly perpendicular to the bar. The x-axis is distance from the bar in arcsec, The y-axis is projected line-of-sight velocity. The lines are the velocity fields of models; all have  $M/L = 2.25$ . The  $\Omega_p$  values are 10.0 (dotted), 14.0 (short dash), 20.0 (solid), and 24.0 (long dash).

1.35, and 0.68.

As the pattern speed is decreased and the Lagrange radius increased, the shock moves upstream, in the direction of rotation of the galaxy and of the bar. This behavior occurs because at slower bar pattern speeds, the gas overtakes the bar more quickly, and climbs farther out of the bar potential before shocking. The higher velocity of the gas in the co-rotating frame also causes the shock to steepen for slower bars, as noted in Section 6. At  $\Omega_p = 10$ , the pattern speed is so slow that the velocity gradient of the shock is extremely steep. This model is so extreme that the global flow pattern changes and the relation between pattern speed and shock location breaks down.

The behavior of models in this pseudo-slit cut through the data shows clearly why the observations favor models with high  $M/L$  and high  $\Omega_p$ . This is also generally true of the models not shown in either Figure 7 or 8. There is some covariance between the parameters  $M/L$  and  $\Omega_p$ , but their effects on the location and gradient of the shock are rather different. The best models have high mass disks and fast bars, and it is not possible to rescue light mass disks with  $M/L < 2.0$  by appealing to slow bars.

## 8. DISCUSSION I. PROPERTIES OF THE DARK HALO

Our measurement of the disk  $M/L$  of NGC 4123 determines the disk mass distribution, and, since we have an extended H I rotation curve, the mass distribution of the dark halo. We find that the disk dominates the mass inside the optical radius  $R_{25}$ ; see the rotation curve decompositions in Paper I for  $M/L = 2.25$ . We have only used data inside the bar radius, but the result is robust: the disk

dominates the mass even if its  $M/L$  were to decline outside the bar radius (Section 6.3 of Paper I). Dark matter halos with either isothermal profiles with a constant-density core, or power-law profiles with an inner cusp, are both consistent with the data, as discussed in Paper I. However, the halo rotation curve  $V_{halo}(R)$  and equivalently the enclosed mass  $M_{halo}(< R)$  are fairly well constrained, especially at large  $R$ . Hence we have detailed knowledge of the radial distribution of luminous and dark mass in this galaxy. In this section we use the mass distributions to test models of the relation between disks and their dark halos, and of the process of disk formation by dissipative collapse within the halo.

### 8.1. Comparison to “universal” relations

The tight correlation between galaxy luminosity and rotation width, the Tully-Fisher relation, suggests that there is some kind of universal relation between galaxy disks and halos, especially since galaxy rotation curves are approximately flat out past the optical radius. Recently there have been a number of suggestions for universal relations which govern the disk-to-halo ratios of galaxies, which can be tested against NGC 4123. Additionally, models of structure formation yield predictions for dark matter halo parameters.

The “Universal Rotation Curve” claimed by Persic, Salucci & Stel (1995) gives a relation of disk and halo mass with rotation velocity, and suggests that galaxies of smaller rotation width are more dark matter dominated. For NGC 4123, their relation predicts that dark matter should become dynamically detectable at  $0.6R_{25}$  (6.7 kpc)

and that the mass within this radius is 40% dark. In contrast, we find that the galaxy is at most 15% dark matter within that radius.

Several studies motivated by cosmological simulations of structure formation have examined the structure of dark matter halos. Such simulations produce centrally concentrated dark halos, generally with a broken-power law density profile, with a central cusp slope of  $r^{-1}$  or  $r^{-1.5}$  (e.g. Navarro *et al.* 1996; Syer & White 1996; Kravtsov *et al.* 1998; Moore *et al.* 1999; Klypin *et al.* 2000). However, these studies do agree that the central concentration of dark halos is dependent on the mass of the halo and on the cosmological model. Such halos follow one-parameter families: the halo scale density and radius are linked.

It is tempting to identify a one-parameter halo family with the Tully-Fisher relation and derive a relation between halo scale and rotation width. Navarro *et al.* (1996) proposed a relation of halo to galaxy which produces galaxies that are very dark matter dominated: a galaxy with a maximum rotation of  $200 \text{ km s}^{-1}$  is 90% dark matter within the optical radius, and a galaxy with maximum rotation of  $100 \text{ km s}^{-1}$  is 96% dark matter within the optical radius.

The  $\Omega = 0.3$  model of Navarro (1998a), where there is less dark matter to go around, still produces very dark matter dominated galaxies. Figure 2 of Navarro (1998a) proposes a disk-halo decomposition of the well-studied galaxy NGC 3198, whose rotation width is about  $150 \text{ km s}^{-1}$ , similar to that of NGC 4123. In the model of Navarro (1998a), NGC 3198 is 75% dark matter inside the optical radius, the dark halo dominates the rotation curve even at 2 kpc from the galaxy center, and the disk  $M/L$  is  $\simeq 0.8h_{75}$ . This model is clearly inconsistent with our result for NGC 4123.

In Figure 9 we plot the (pre-baryonic-collapse) halo scale density and radius predicted for a galaxy of circular velocity  $V_c = 130 \text{ km s}^{-1}$  from the models of Navarro (1998b), and the confidence ellipses for our NFW-type halo fits to the H I rotation curve of NGC 4123, from Paper I. In all cases, for disk  $M/L$  from 2.0 to 2.5 and for all three cosmologies, the halos determined by our modeling have lower scale density or radius (or both) than the CDM halo predictions. The implication is that either the dark halo is of similar size to the prediction but less dense by a factor of  $\sim 3$ , or the dark halo has a smaller break radius than predicted. Since the inner part of an NFW-type halo has  $\rho \sim r^{-1}$ , a smaller scale radius means a lower halo density at a given physical radius in kpc. In terms of the NFW halo concentration parameter  $c$ , we find that the halo of NGC 4123 has  $c = 2.1$ , while Navarro (1998b) predicted  $c \simeq 5$  for the  $\Lambda$ CDM cosmology with  $\Omega_M = 0.3$ .

The study of Bullock *et al.* (1999) uses a large number of simulated halos to determine the  $c - M$  relation and scatter. Although it does not directly propose disk-halo decompositions, we can find the concentration expected for the halo of NGC 4123. In a  $\Lambda$ CDM cosmology, the halo has a mass of  $M_{\text{vir}} = 3 \times 10^{11} M_\odot$  for an NFW-type profile. Using a modified definition of the concentration,  $c_{\text{vir}}$ , Bullock *et al.* predict that such a halo will have  $c_{\text{vir}} = 16.6$  in a  $\Lambda$ CDM model, and the scatter is given by  $\log c_{\text{vir}} = 1.22 \pm 0.14$ . The halo of NGC 4123 has  $c_{\text{vir}} = 4.4$ , or  $\log c_{\text{vir}} = 0.64$ , a  $4\sigma$  deviation, requiring a much less dense halo than predicted.

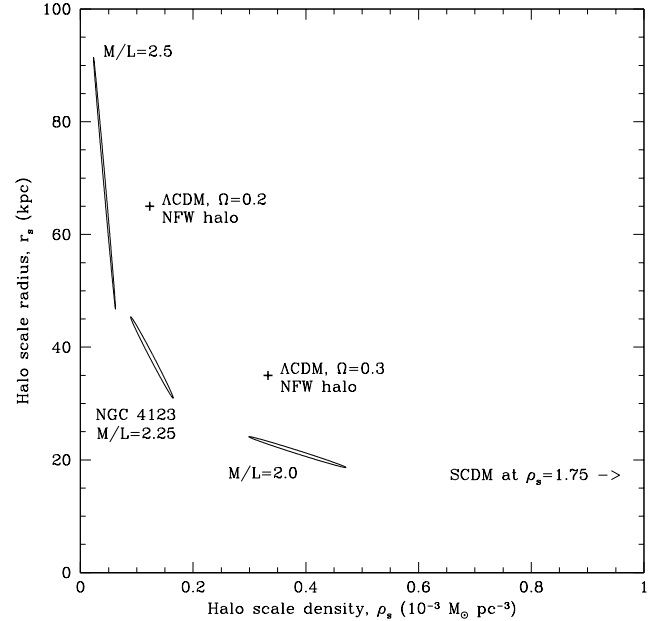


FIG. 9.— Parameters of the dark halo vs. predictions. The scale density  $\rho_s$  and radius  $r_s$  of the NFW-type dark halos allowed by our models compared to the pre-collapse halos predicted by the simulations of Navarro (1998b). The  $1\sigma$  confidence ellipses in  $\rho_s - r_s$  space determined from our rotation curve fits in Paper I are shown for the allowed disk  $M/L$  from 2.0 to 2.5. The halo parameters predicted for a galaxy of NGC 4123's rotation width are indicated for three cosmologies.

We emphasize that the dark halo we determine by fitting the rotation curve is seen in its final state, after the baryonic disk has collapsed inside it. The dissipative baryonic collapse must draw the halo inward so that the final halo has a higher density and smaller radius than the initial state. The halo parameter predictions from Navarro (1998b) and Bullock *et al.* (1999) are pre-collapse halos, which increases the discrepancy between the predictions and our measurements of halo concentration. In the next section we describe an attempt to quantify the effects of baryonic collapse.

## 8.2. Baryonic collapse and the initial halo density profile

The dominant paradigm of disk galaxy formation requires that the baryonic disk collapse within the dark matter potential, drawing the halo inward (White & Rees 1978; Fall & Efstathiou 1980; Faber 1981). The final disk and halo mass distributions, which we have measured in the form of  $V_{\text{disk}}(R)$  and  $V_{\text{halo}}(R)$ , can in principle be used to infer the initial, pre-collapse halo density profile, which is clearly of great interest. We show here that using the standard prescription to approximate the collapse process leads to an unrealistic initial profile. A more sophisticated treatment of the collapse will be needed to determine the initial density profile of the dark halo from rotation curve information.

It is generally assumed that collapse into a galaxy is a two-stage process: first the halo (dark matter and baryons) forms, then the baryonic component cools within the dark matter halo, contracting until it is halted by angular momentum (Fall & Efstathiou 1980). The dis-

Halo type	Scale density $10^{-3} \text{ M}_\odot \text{ pc}^{-3}$	Scale radius kpc
Isothermal	4.68	6.33
NFW-type	0.127	38.2
Moore-type	0.040	61.0

TABLE 2

HALO MODELS: BEST-FIT PARAMETERS FOR  $M/L_I = 2.25$ 

sipative baryonic collapse compresses the dark halo. The formalism often used to model this collapse is known as the adiabatic-compression or circular-orbit approximation (see *e.g.* Faber 1981; Blumenthal *et al.* 1986). This formalism is an integral part of many recent treatments of the process of disk formation (Dalcanton, Spergel & Summers 1997; Mo, Mao, & White 1998; van den Bosch 1998, 2000; Navarro & Steinmetz 2000), which compute the final state of the disk from its angular momentum distribution, and use the adiabatic-compression formalism to compute the post-collapse dark halo mass profile.

The formalism assumes that (1) the disk can be approximated by a sphere with the same enclosed-mass profile; (2) the collapse of the disk inside the halo is roughly adiabatic; (3) that detailed conservation of angular momentum applies; and (4) that “mass shells don’t cross,” i.e. that dark halo particles behave as if they were all on circular orbits. Under these assumptions, the initial and final halos are related by

$$r_i M_{i,\text{total}}(r_i) = r_f (M_{f,\text{disk}}(r_f) + M_{f,\text{halo}}(r_f)) \quad (2)$$

where  $M(r)$  indicates the mass interior to  $r$ , and subscripts  $i$  and  $f$  indicate initial and final quantities. The halo mass shell originating at  $r_i$  ends up at  $r_f$ . This equation assumes the conservation of angular action, which holds for individual dark matter particles, but in order to apply it to mass shells one has to assume that mass shells have a well-defined radius and that they do not cross. For this reason we prefer to call the formalism a circular-orbit approximation, although many authors simply refer to it as “adiabatic compression” of the halo by the disk.

Our determination of the disk  $M/L$ , and of the halo parameters from the H I rotation curve, give us the final mass profiles of both the disk and the halo. From this it is easy to use Equation 2 to find the radius  $r_i$  corresponding to each  $r_f$  (i.e. the collapse factor at each radius) and the initial mass profile  $M_i(r_i)$ , the decompressed halo. We carried this out for models with a  $M/L = 2.25$  stellar disk and the corresponding isothermal and NFW-type final dark-halo profiles  $M_{f,\text{halo}}(r_f)$ .

The final profiles must be more centrally concentrated than the initial profiles, so we also fit a very centrally concentrated final halo to the rotation curve and decompressed that model, using a “Moore-type” halo profile with a central density cusp of  $\rho \propto r^{-1.5}$  (Moore *et al.* 1999). The parameters of the fitted final dark halos are given in Table 2. The very centrally concentrated Moore-type halo can make an acceptable fit to the data, but only at the price of a quite large scale radius.

The assumption that mass shells don’t cross implies that  $M_{i,\text{halo}}(r_i) = M_{f,\text{halo}}(r_f)$ . Then the halo can be “decom-

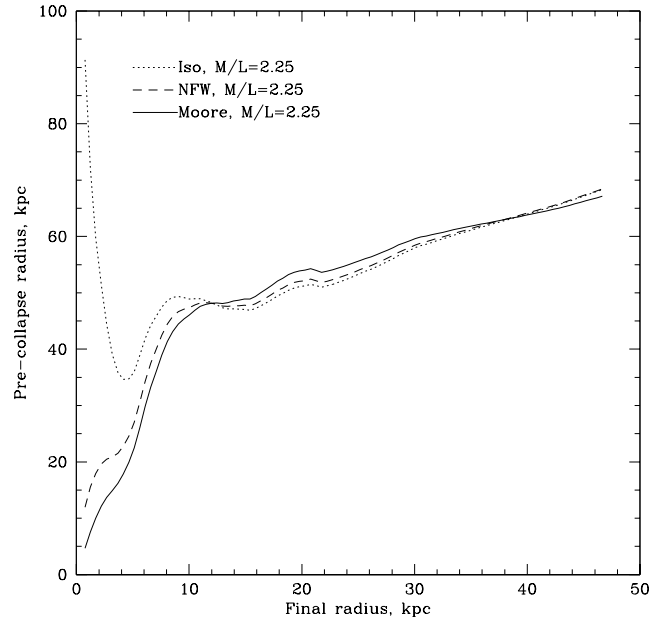


FIG. 10.— Halo compression in the circular-orbit approximation. The initial, pre-collapse radius  $r_i$  of a halo mass shell, obtained using the circular-orbit formalism to uncompress the halo, plotted against its final radius  $r_f$ . The three models have final halo profiles of isothermal (dotted), NFW-type (dashed), and Moore-type (solid).

pressed” by solving Equation 2 for the initial radius. Using assumption (1) above, we approximate the disk by a sphere and convert from  $M_{f,\text{disk}}$  to  $V_d$ :

$$\frac{r_i}{r_f} = (1 - f_b) \left( 1 + \frac{V_d^2(r_f)}{V_h^2(r_f)} \right) \quad (3)$$

where  $f_b$  is the baryon fraction, i.e.  $M_{i,\text{disk}} = f_b M_{i,\text{total}}$ , and  $V_d$  includes the stellar and H I disks. The effect of the spherical assumption is small (Barnes 1987; Sellwood 1999). We assumed a baryon fraction of 0.1; different values of  $f_b$  have little effect on the results, since they just change the scale of  $r_i$ .

Figure 10 shows the initial radius as a function of final radius for the isothermal, NFW-type, and Moore-type halos. The predominant feature is a break at  $r_f \sim 9$  kpc, which is the location of the peak in the disk rotation curve (see Paper I). Inside  $R = 9$  kpc,  $V_d$  increases steeply, while outside 9 kpc,  $V_d$  drops as  $V_h$  rises gently. Outside 9 kpc, the results for all models are nearly identical.

At small radii in the isothermal halo model,  $r_f$  is not a monotonic function of  $r_i$ , which means that the assumption that mass shells do not cross is not self-consistent. Under the assumption of the adiabatic circular-orbit approximation, there is no initial halo profile which can yield a final isothermal halo profile for NGC 4123.

In the NFW and Moore-type halo models,  $r_f(r_i)$  does not strongly violate monotonicity. There are a few bumps, at  $r_i = 3, 9$ , and 20 kpc, which are clearly related to small-scale features in the stellar+gas rotation curve (see Figure 8 of Paper I) and do not represent real features in the collapse profile of the dark halo.

The upper panel of Figure 11 shows the final enclosed-mass profiles of the three halo models, determined by fit-



ting the rotation curve. Since all three models are determined by the same data, they are very similar, except in the central 10 kpc, where the rotation curve is dominated by the stellar disk and the halo is not well constrained.

The lower panel of Figure 11 shows the enclosed-mass profiles of the initial, uncompressed halos derived from the three halo models. The initial halos are much less concentrated than the final halos. For the final isothermal halo, the initial mass profile is unphysical, because  $r_i(r_f)$  is not monotonic. For the final NFW and Moore-type profiles, the initial profiles are essentially physical, with small deviations due to the wiggles in  $r_i(r_f)$  caused by structure in the disk+gas rotation curve.

Outside  $r_i \sim 47$  kpc, the mass profiles of all three models are similar, even for the final isothermal halo. Figure 10 shows that this radius corresponds to  $r_f = 9 - 10$  kpc, the location of the peak of the stellar+gas rotation curve. Inside this radius, the halo profile is not strongly constrained, and the uncompression is influenced by features in the stellar distribution. Outside this radius, the halo profile is fairly well constrained by the need to fit the H I rotation curve; the fitted final mass profiles for isothermal, NFW, and Moore profiles are similar; and the initial mass profiles in the three models are also similar.

The derived initial mass profile outside  $r_i = 50$  kpc is well described by a power law:  $M_{i,halo} \propto r_i^{3.3}$ , implying an initial density profile of  $\rho_i \propto r_i^{-0.3}$ , extending out to  $r_i \simeq 70$  kpc. Inside 50 kpc, this power law also fits the initial profile for the NFW model; the Moore model is shallower while the isothermal model becomes unphysical.

A  $\rho \propto r^{-0.3}$  density profile for the pre-galactic initial overdensity is extremely unattractive. The problem exists in all three halo models; it is simply a consequence of the relative disk and halo rotation curves and Equation 3. The initial mass profile is actually best determined at large radius, while a roughly constant density would only be believable in *e.g.* the inner core of the pre-galactic halo.

We believe that the problem is in the circular-orbit formalism, which can exaggerate the amount of halo collapse caused by a high mass disk (Barnes 1987; Sellwood 1999). The assumption most likely to be violated is that mass shells do not cross, since a real halo will have some fraction of radial orbits; radial orbits can provide extra stiffness against compression (Barnes 1987). It is also possible that detailed conservation of angular momentum is violated, *e.g.* through angular momentum transfer within or between disk and halo, or through mass loss. However, transfer of angular momentum from disk to halo would exacerbate the overcooling problem found in CDM+gas simulations, which results in disks that are too small (*e.g.* Navarro & Steinmetz 1997, 2000).

In order to produce the relatively low density and large scale radius final halos that we obtained from fitting the rotation curve, the circular-orbit approximation forces an unrealistically diffuse initial condition. The use of the circular-orbit formalism to calculate properties of observed galaxies could be misleading. It should be possible in future work to derive the initial halo properties from measured final disk and halo mass profiles, through either  $N$ -body simulation or analytic models with more complex dynamics (*e.g.* a model incorporating a halo distribution function, and in which both angular and radial actions are conserved during compression).

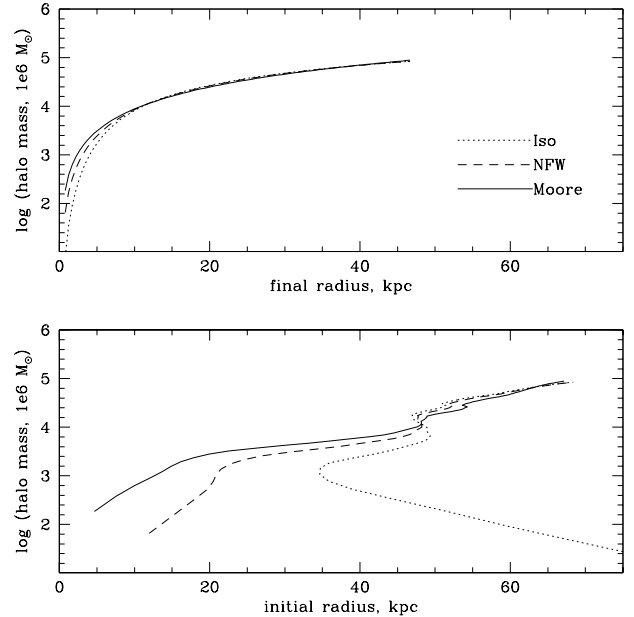


FIG. 11.— Initial and final halo mass profiles in the circular-orbit approximation. Upper panel: Final halo enclosed-mass profiles  $\log M_{f,halo}(r_f)$  determined by fitting the rotation curve, for three model halo profiles: isothermal (dotted), NFW-type (dashed), and Moore-type (solid line). Lower panel: Initial halo enclosed-mass profiles  $\log M_{i,halo}(r_i)$  obtained using the circular-orbit uncompression formalism. Line styles as above. The isothermal model is unphysical inside 35 kpc (see text).

## 9. DISCUSSION II. IS NGC 4123 TYPICAL?

The comparisons between the observed velocity field of the bar in NGC 4123 and the gas-dynamical models show conclusively that: (1) the stellar disk of the galaxy is high-mass, in the sense of being close to maximum disk, implying that the disk dominates the rotation curve until well outside the optical radius of the galaxy; and (2) the bar rotates quickly. These conditions are required to match the strength and location of the shock observed in the bar.

We found that NGC 4123 has a disk  $I$ -band mass-to-light ratio of 2.0 – 2.5 (times  $h_{75}$ ), and is dominated by the stellar disk within the optical radius. The best value for disk  $M/L_I$  is 2.25, and  $M/L_I = 2.0$  is a hard lower limit. Examining the mass models in Figure 8 of Paper I shows that for a disk  $M/L = 2.25$ , the stellar disk contribution reaches 87% of the total rotation velocity at the optical radius  $R_{25}$  of 11.1 kpc, or 76% of the centripetal acceleration at that radius. The disk fraction of the mass inside  $R_{25}$  is slightly lower, since disk flattening boosts its contribution to the centripetal acceleration: the stellar disk is 72% of the mass inside  $R_{25}$ . The gas disk is responsible for another 5% of the mass inside  $R_{25}$ . The dark halo, when assumed to be spherical, is 23% of the mass inside a sphere of radius  $R_{25}$ . Table 3 summarizes the mass fractions for models with  $M/L_I = 2.0$  to 2.5. In all, the stellar disk is quite dominant inside  $R_{25}$ .

We note that an error in the distance to NGC 4123 would affect our numerical value of  $M/L$ , but would not affect our estimate of the degree of maximality of its disk. A larger distance  $D$  reduces the disk  $M/L$ , with

Disk $M/L_I$	Component	Fraction of	
		$V_{rot}^2$	Mass
All	Gas disk	0.06	0.05
2.00	Stellar disk	0.66	0.63
...	Dark halo	0.28	0.31
2.25	Stellar disk	0.76	0.72
...	Dark halo	0.18	0.23
2.50	Stellar disk	0.83	0.79
...	Dark halo	0.11	0.16

TABLE 3  
DISK AND HALO FRACTIONS WITHIN  $R_{25}$

NOTE.— Fractions of rotation velocity squared and of mass within a sphere of radius  $R_{25}$  (11.1 kpc). The mass fractions for the dark halo assume that it is spherical.

$M/L \propto D^{-1}$ , but maintains the disk contribution to the rotation curve since  $L$  goes up.

The result that NGC 4123 has a high-mass stellar disk and a low-concentration dark halo is interesting in itself, since it strongly violates a number of nominally-universal predictions for the properties of dark halos of galaxies, as described in the previous section. However, it is clearly important to know whether the result applies to disk galaxies in general.

### 9.1. The Tully-Fisher relation

Perhaps the strongest argument that NGC 4123 is typical is its place on the Tully-Fisher relation. As described in Paper I, NGC 4123 is 0.2 mag more luminous than the mean  $I$ -band Tully-Fisher relation for galaxies of type Sbc and later, which has an intrinsic scatter of 0.3 mag (Giovannelli *et al.* 1997). One could interpret its overluminosity as a sign that its  $M/L$  is 20% off the mean, or that it has 20% more luminous matter than the mean, or as a 10% overestimate of its distance. None of these possibilities bring NGC 4123 significantly closer to the theoretical models. In any case the overluminosity is not statistically significant.

Scenarios in which most galaxies have a substantial amount of dark matter inside the optical radius and NGC 4123 is an outlier are unappetizing. A galaxy at the same place on the TF relation but with  $\sim 50\%$  dark matter inside the optical radius would have to have a stellar  $M/L$  different by nearly a factor of 2. If stellar  $M/L$  varied by such a large amount, the TF relation would have a much larger scatter than is observed.

### 9.2. Barred galaxies

Is NGC 4123 typical of barred galaxies? Strongly barred galaxies generally show straight, offset dust lanes like those in NGC 4123 (see Athanassoula 1992); many examples can be found in the standard atlases (*e.g.* Sandage 1961; Sandage & Bedke 1988). Spectroscopic studies of strongly barred galaxies show large velocity jumps associated with these dust lanes, as in Figure 5 of Paper I, NGC 1365 (Lindblad & Jörsäter 1987, Lindblad *et al.* 1996) and NGC 1530 (Regan *et al.* 1997). The dust lanes indicate the location of shocks, as discussed above and in Paper I.

The position of the dust lanes favors fairly fast-rotating bars; in slow bars the shocks move too far ahead of the bar, as seen in the simulations presented here and the simulations of the Milky Way presented by Weiner & Sellwood (1999). The most secure dynamical determinations of bar pattern speeds in other galaxies also indicate that NGC 936 and NGC 4596 have fast-rotating bars, with corotation just outside the end of the bar (Merrifield & Kuijken 1995; Gerssen *et al.* 1999; using the method of Tremaine & Weinberg 1984).

The presence of shocks indicates the disk  $M/L$  is likely to be high; if the dark matter halo dominates the rotation curve, the potential is too round to produce strong shocks, as can be seen from our  $M/L = 1.0$  simulation (Figures 2 and 7). Furthermore, a high disk  $M/L$  is also implied by fast-rotating bars, since otherwise the bar which forms in a heavy halo is quickly slowed by dynamical friction, as discussed in Section 2 (Weinberg 1985, Debattista & Sellwood 1998).

### 9.3. What about unbarred galaxies?

NGC 4123 is strongly barred. Since bars can form by instabilities in massive disks, but the instability can be deterred by a massive halo, it has been argued that unbarred galaxies require massive halos (*e.g.* Ostriker & Peebles 1973; Efstathiou, Lake & Negroponte 1982). Conversely one could argue that barred galaxies are preferentially disk dominated. However, it takes a lot of halo to deter bar formation: as noted by Kalnajs (1987), central bulges are more efficient than extended dark halos at stabilizing disks. Adding more halo mass in the form of spherical shells at large radius has zero effect on the dynamics of the matter interior to those shells, so stabilizing a disk with a halo requires cranking up the central density. Additionally, bars can form in disks with massive halos (see *e.g.* Combes & Sanders 1981, Debattista & Sellwood 1998). But is NGC 4123 a self-selected exception by virtue of being strongly barred?

First, relations which claim universality should clearly apply to unexceptional galaxies, and NGC 4123 is quite ordinary, especially given its modest rotation width. Some 30% of galaxies in major catalogs are classified as barred, plus some percentage of intermediate types (Sellwood & Wilkinson 1993), and an even larger bar fraction is found from infrared imaging (Eskridge *et al.* 2000). It seems unsatisfying to put forward galaxy formation scenarios which exclude such a large percentage of observed galaxies.

There are no differences in the overall H I properties of barred and unbarred galaxies (Bosma 1996). Palunas (1996) finds that maximum disk fits to galaxy rotation curves yield a median  $I$ -band  $M/L$  of  $(2.4 \pm 0.9)h_{75}$ , very close to our value for NGC 4123. The distributions of maximum disk  $M/L$  for barred and unbarred galaxies in Palunas's sample are indistinguishable (Sellwood 1999).

We are unaware of any evidence that barred and unbarred galaxies fall on different Tully-Fisher relations. Many Tully-Fisher surveys tend to avoid selecting barred galaxies. However, Figure 1 of Syer, Mao & Mo (1999) plots a measure of total (disk+halo) mass-to-light ratio versus central surface brightness – a variant of the Tully-Fisher relation – for the 2446 galaxies for which Mathewson & Ford (1996) obtained rotation curves and  $I$ -band photometry. 175 of these galaxies were classified as barred.

There is no difference in the distribution of barred versus unbarred galaxies, implying that the barred and unbarred galaxies do have similar luminosities at the same velocity width (see also Sellwood 1999). Syer *et al.* nevertheless argued that disk galaxies should have low mass disks,  $M/L \lesssim 1.4h_{75}$ , in order to satisfy a stability criterion designed to deter bar formation.

It is extremely difficult to understand how barred and unbarred galaxies could lie on the same T-F relation and have similar maximum disk  $M/L$  and H I properties, yet have true disk mass-to-light ratios varying by a factor of 2-3. In fact, Syer *et al.* themselves do not favor such an approach – they argued that perhaps disks have a critical value of  $M/L$ , so that bars do not form spontaneously, but can form when induced by *e.g.* encounters between galaxies. This argument is not particularly compelling, especially in light of the high disk  $M/L$  of NGC 4123 and the dynamical friction argument for high disk  $M/L$  in most barred galaxies (Debattista & Sellwood 1998).

Relying on extremely dominant halos to deter bar formation leads to an division between barred and unbarred galaxies for which there is no evidence, and in which the existence of intermediate types is hard to understand. Bar formation can be deterred by other means than a heavy halo; Kalnajs (1987) emphasized the importance of bulges in stabilizing disks (see also Sellwood & Evans 2000). Bars can be deterred by a central mass dense enough to cause an inner Lindblad resonance (Toomre 1981) or destroyed by a relatively small mass accumulation at the center of the bar, which can arise naturally as the bar torque drives gas to the center (Pfenniger & Norman 1990, Hasan *et al.* 1993, Friedli & Benz 1993, Norman *et al.* 1996). Many unbarred galaxies with large bulges may have once had bars, and whether a high-surface-brightness galaxy is barred or unbarred today may depend more on its formation history than on its disk/halo ratio (Sellwood & Moore 1999).

The high disk  $M/L$  of NGC 4123, with its modest rotation width, suggests that the common picture in which lower rotation width galaxies are more dark matter dominated may not be correct for high surface brightness galaxies. Low surface brightness galaxies appear to be quite dark matter dominated (de Blok & McGaugh 1996, 1997; Swaters *et al.* 2000) and surface brightness, rather than rotation width, is likely to be the sequence along which dark matter content varies. Detailed models of galaxy formation predict that specific angular momentum, not mass, is the parameter which controls the baryon collapse factor, so that a galaxy with larger angular momentum is both more spread out (lower surface brightness) and has less baryonic mass within a given number of scale lengths (more dark matter dominated, and higher total  $M/L$ ) (Dalcanton *et al.* 1997).

## 10. CONCLUSIONS

Comparing the observed non-circular motions in NGC 4123 to simulations of gas flow in model potentials, derived directly from the light distribution, shows that the galaxy has a high mass disk and a fast-rotating bar. The best match between simulations and data is for an  $I$ -band disk  $M/L$  of 2.25 and a bar pattern speed  $\Omega_p$  of  $20 \text{ km s}^{-1} \text{ kpc}^{-1}$ , implying a Lagrange radius  $r_L$  of 1.35 times the bar semimajor axis  $a$ . The acceptable range of

the  $I$ -band disk  $M/L$  is 2.0 – 2.5. The maximum disk value is 2.5 for a disk in an isothermal halo, or 2.25 for a disk in a power-law halo similar to the NFW profile, so the galaxy is 80 – 100% of the maximal disk. The acceptable range of  $\Omega_p$  is from 18 to 24, implying that  $r_L/a < 1.5$ .

Lighter disks can be excluded because they do not produce shocks as strong as those observed. Slower bars can be excluded because the shock occurs in a location which does not match the observations: slower bars produce a shock which is farther ahead of the bar, in the direction of galactic rotation.

The observed shocks occur at the location of straight offset dust lanes of the type commonly seen in strong bars (Athanasoulas 1992). The ubiquity of these dust lanes suggests that strong bars generally rotate quickly, otherwise the shocks would occur in the wrong place. Fast-rotating bars imply near-maximal disks, since in halo-dominated disks the bar is slowed by dynamical friction (Weinberg 1985; Debattista & Sellwood 1998). Low mass disks also do not produce shocks which extend the length of the bar, unless the pattern speed is very slow, in which case the shocks are again too far ahead of the bar. These results suggest that strongly barred galaxies have high mass disks and fast-rotating bars.

The near-maximal disk of NGC 4123 does not agree with a number of predictions which suggest that galaxies with rotation curve height  $\simeq 130 \text{ km s}^{-1}$  should be dominated by dark matter inside the optical radius (*e.g.* Persic *et al.* 1996; Navarro 1998b) nor with predictions that disk galaxies must have low  $M/L$  to satisfy stability criteria (*e.g.* Efstathiou *et al.* 1982). The high disk  $M/L$  can be consistent with a power-law NFW-type halo, but the halo must be much less dense than predicted by the relations between halo concentration and mass found in CDM and  $\Lambda$ CDM simulations (Navarro *et al.* 1996; Bullock *et al.* 1999). When we attempt to derive the initial state of the halo from the adiabatic compression and circular-orbit formalism commonly used to model disk collapse within a dark halo (Faber 1981; Blumenthal *et al.* 1986), the inferred initial density profile goes as  $r^{0.3}$ . This unrealistic halo profile indicates a failure of the circular-orbit approximation.

Though NGC 4123 is barred, there is no sign that barred galaxies are more disk dominated than unbarred galaxies, at least for high surface brightness galaxies; their Tully-Fisher relations and total mass-to-light ratios are similar. Requiring heavy halos to stabilize disks is not necessary, since bars can also be deterred or destroyed by central bulges. The ultimate question of why some galaxies are barred and some unbarred remains unsettled, but dark halo mass is not the controlling factor.

We have shown that the noncircular motions in a barred galaxy can be used to determine the  $M/L$  of its stellar component. Together with H I observations, these can be used to constrain the radial density profile of the galaxy's dark matter halo. While not every barred galaxy is suitable for the modeling process outlined here, observations and modeling of more galaxies will eventually lead us to determinations of stellar  $M/L$  and dark halo parameters for galaxies as a function of their rotation width, surface brightness, and position on the Hubble sequence.

We thank Jacqueline van Gorkom for her contributions

to and support of this project, Dick van Albada and Lia Athanassoula for providing the fluid-dynamical code and for comments on its use, Povilas Palunas and Julianne Dalcanton for many helpful conversations and encouragement, and Jason Prochaska and the anonymous referee for comments which improved the manuscript. This research was supported in part by NSF grant AST 96/17088 and NASA LTSA grant NAG 5-6037 to JAS, and by NSF grant AST 96-19510 to TBW. BJW has been supported by a Barbara McClintock postdoctoral fellowship from the Carnegie Institution of Washington.

## REFERENCES

- Athanassoula, E. 1992, *MNRAS*, 259, 345  
Athanassoula, E., Bosma, A., & Papaioannou, S. 1987, *A&A*, 179, 23  
Bahcall, J.N., & Casertano, S. 1985, *ApJL*, 293, L7  
Barnes, J. 1987, in *Nearly Normal Galaxies*, ed. Faber, S.M. (New York: Springer), 154  
Begeman, K. 1987, PhD thesis, Groningen University  
Binney, J. 1991, *ARAA*, 30, 51  
Binney, J., & Merrifield, M. 1998, *Galactic Astronomy*, (Princeton: Princeton U.P.)  
Binney, J., & Tremaine, S. 1987, *Galactic Dynamics*, (Princeton: Princeton U.P.)  
Blumenthal, G.R., Faber, S.M., Flores, R., & Primack, J.R. 1986, *ApJ*, 301, 27  
Bosma, A. 1996, in *Barred Galaxies*, IAU Colloquium 157, ed. Buta, R., Crocker, D.A., & Elmegreen, B.G. (San Francisco: A.S.P.), 197  
Bosma, A. 1999, in *Galaxy Dynamics*, ed. Merritt, D.R., Valluri, M., & Sellwood, J.A. (San Francisco: A.S.P.), 339  
Bottema, R. 1993, *A&A*, 275, 16  
Bottema, R. 1997, *A&A*, 328, 517  
Broeils, A.H. & Courteau, S. 1997, in *Dark and Visible Matter in Galaxies*, ed. Persic, M. & Salucci, P. (San Francisco: A.S.P.), 74  
Bullock, J.S., Kolatt, T.S., Sigad, Y., Somerville, R.S., Kravtsov, A.V., Klypin, A.A., Primack, J.R., & Dekel, A. 1999, preprint astro-ph/9908159  
Bureau, M. & Freeman, K. C. 1999, *AJ*, 118, 126  
Casertano, S. & van Gorkom, J. H. 1991, *AJ*, 101, 1231  
Combes, F., & Sanders, R.H. 1981, *A&A*, 96, 164  
Courteau, S., & Rix, H.-W. 1999, *ApJ*, 513, 561  
Dalcanton, J.J., Spergel, D.N., & Summers, F.J. 1997, *ApJ*, 482, 659  
de Blok, W.J.G., & McGaugh, S.S. 1996, *ApJL*, 469, L89  
de Blok, W.J.G., & McGaugh, S.S. 1997, *MNRAS*, 290, 533  
de Grijs, R. 1997, PhD thesis, Groningen  
de Grijs, R., & van der Kruit, P.C. 1996, *A&AS*, 117, 19  
Debatista, V.P. & Sellwood, J.A. 1998, *ApJL*, 493, L5  
Dettmar, R.-J., & Barteldrees, A. 1990, in *ESO/CTIO Workshop on Bulges of Galaxies*, ed. Jarvis, B.J., & Terndrup, D.M. (Garching: ESO), 259  
Duval, M.F., & Athanassoula, E. 1983, *A&A*, 121, 297  
Efsthathiou, G., Lake, G. & Negroponte, J. 1982, *MNRAS*, 199, 1069  
Elmegreen, B.G. 1996, in *Barred Galaxies*, IAU Colloquium 157, ed. Buta, R., Crocker, D.A., & Elmegreen, B.G. (San Francisco: A.S.P.), 197  
Englmaier, P., & Gerhard, O. 1997, *MNRAS*, 287, 57  
Eskridge, P.B., *et al.* 2000, *AJ*, 119, 536  
Faber, S.M. 1981, in *Astrophysical Cosmology: Proceedings of the Study Week on Cosmology and Fundamental Physics*, ed. Brück, H.A., Coyne, G.V., & Longair, M.S. (Vatican City: Pontificia Academia Scientiarum), 191  
Fall, S.M., & Efsthathiou, G. 1980, *MNRAS*, 193, 189  
Freeman, K.C. 1992, in *Physics of Nearby Galaxies: Nature or Nurture?*, ed. Thuan, T.X., Balkowski, C., & Van, J.T.T. (Gif-sur-Yvette: Editions Frontieres), 201  
Friedli, D., & Benz, W. 1993, *A&A*, 268, 65  
Fuchs, B. 1999, in *Galaxy Dynamics*, ed. Merritt, D.R., Valluri, M., & Sellwood, J.A. (San Francisco: A.S.P.), 365  
Fux, R. 1999, *A&A*, 345, 787  
Gerssen, J., Kuijken, K. & Merrifield, M. R. 1999, *MNRAS*, 306, 926  
Giovannelli, R., Haynes, M.P., Herter, T., Vogt, N.P., Wegner, G., Salzer, J.J., Da Costa, L.N., & Freudling, W. 1997, *AJ*, 113, 53  
Gunn, J.E., Knapp, G.R., & Tremaine, S.D. 1979, *AJ*, 84, 1181  
Hassan, H., Pfenniger, D., & Norman, C. 1993, *ApJ*, 409, 91  
Hockney, R.W. 1965, *J. Assoc. Comp. Mach.* 12, 95  
Jenkins, A., & Binney, J. 1994, *MNRAS*, 270, 703  
Kalnajs, A. 1983, in *Internal Kinematics and Dynamics of Disk Galaxies*, IAU Symposium 100, ed. Athanassoula, E. (Dordrecht: Reidel), 87  
Kalnajs, A. 1987, in *Dark Matter in the Universe*, IAU Symposium 117, ed. Kormendy, J., & Knapp, G.R. (Dordrecht: Reidel), 289  
Kent, S.M. 1986, *AJ*, 91, 1301  
Klypin, A., Kravtsov, A.V., Bullock, J.S., & Primack, J.R. 2000, preprint astro-ph/0006343  
Kormendy, J., & Richstone, D. 1995, *ARAA*, 33, 581  
Kravtsov, A.V., Klypin, A.A., Bullock, J.S., & Primack, J.R. 1998, *ApJ*, 502, 48  
Kuijken, K. & Gilmore, G. 1991, *ApJL*, 367, L9  
Kuijken, K., & Merrifield, M.R. 1995, *ApJL*, 443, L13  
Lindblad, P.O. & Jorsater, S. 1987, in *Proc. 10th European Regional Astronomy Meeting of the IAU*, (Ondrejov, Czechoslovakia: Czech Acad. Sci.) 4, 289  
Lindblad, P.A.B., Lindblad, P.O., & Athanassoula, E. 1996, *A&A*, 313, 65  
Maller, A., Simard, L., Guhathakurta, P., Hjorth, J., Jaunsen, A.O., Flores, R.A., & Primack, J.R. 2000, *ApJ*, 533, 194  
Martin, P. & Roy, J.-R. 1994, *ApJ*, 424, 599  
Mathewson, D.S. & Ford, V.L. 1996, *ApJS*, 107, 97  
McGaugh, S.S., Schombert, J.M., Bothun, G.D., & de Blok, W.J.G. 2000, *ApJ*, 533, L99  
Merrifield, M.R., & Kuijken, K. 1995, *MNRAS*, 274, 933  
Mihalas, D., & Binney, J. 1981, *Galactic Astronomy*, (New York: Freeman)  
Mo, H.J., Mao, S., & White, S.D.M. 1998, *MNRAS*, 295, 319  
Moore, B., Quinn, T., Governato, F., Stadel, J. & Lake, G. 1999, *MNRAS*, 310, 1147  
Navarro, J.F. 1998a, in *Galactic Halos: a UC Santa Cruz workshop*, ed. Zaritsky, D., (San Francisco: A.S.P.), 409  
Navarro, J.F. 1998b, preprint astro-ph/9807084  
Navarro, J.F., Frenk, C.S., & White, S.D.M. 1996, *ApJ*, 462, 563  
Navarro, J.F., & Steinmetz, M. 1997, *ApJ*, 478, 13  
Navarro, J.F., & Steinmetz, M. 2000, *ApJ*, 528, 607  
Norman, C.A., Sellwood, J.A., & Hasan, H. 1996, *ApJ*, 462, 114  
Olling, R.P. 1996, *AJ*, 112, 457  
O'Neil, K., Bothun, G.D., & Schombert, J. 2000, *AJ*, 119, 136  
Oort, J.H. 1932, *Bull. Astron. Inst. Netherlands*, 6, 349  
Ostriker, J.P., & Peebles, P.J.E. 1973, *ApJ*, 186, 467  
Palunas, P. 1996, PhD thesis, Rutgers University  
Persic, M., Salucci, P. & Stel, F. 1996, *MNRAS*, 281, 27  
Pfenniger, D., & Norman, C. 1990, *ApJ*, 363, 391  
Prendergast, K.H. 1983, in *Internal Kinematics and Dynamics of Galaxies*, IAU Symposium 100, ed. Athanassoula, E. (Dordrecht: Reidel), 215  
Quillen, A.C., Frogel, J.A., & Gonzalez, R.A. 1994, *ApJ*, 437, 162  
Quillen, A.C., & Frogel, J.A. 1997, *ApJ*, 487, 603  
Raha, N., Sellwood, J.A., James, R.A., & Kahn, F.D. 1991, *Nature*, 352, 411  
Regan, M.W., Vogel, S.N., & Teuben, P.J. 1997, *ApJL*, 482, L143  
Sackett, P.D. 1997, *ApJ*, 483, 103  
Sandage, A. 1961, *The Hubble Atlas of Galaxies*, (Washington: Carnegie Inst. of Washington)  
Sandage, A., & Bedke, J. 1988, *Atlas of Galaxies: Useful for Measuring the Cosmological Distance Scale*, (Washington: NASA, US GPO)  
Sellwood, J.A. 1999, in *Galaxy Dynamics*, ed. Merritt, D.R., Valluri, M., & Sellwood, J.A. (San Francisco: A.S.P.), 351  
Sellwood, J.A. & Evans, W. 2000, *ApJ*, submitted  
Sellwood, J.A. & Moore, E.M. 1999, *ApJ*, 510, 125  
Sellwood, J.A. & Sparke, L.S. 1988, *MNRAS*, 231, 25P  
Sellwood, J.A. & Wilkinson, A. 1993, *Rep. Prog. Phys.*, 56, 173  
Sprayberry, D., Bernstein, G.M., Impey, C.D. & Bothun, G. D. 1995, *ApJ*, 438, 72  
Swaters, R.A., Madore, B.F. & Trewheila, M. 2000, *ApJ*, 531, L107  
Syer, D. & White, S. D. M. 1998, *MNRAS*, 293, 337  
Syer, D., Mao, S., & Mo, H.J. 1999, *MNRAS*, 305, 357  
Teuben, P.J., & Sanders, R.H. 1985, *MNRAS*, 212, 257  
Toomre, A. 1981, in *Structure and Evolution of Nearby Galaxies*, ed. Fall, S.M., & Lynden-Bell, D. (Cambridge: Cambridge U.P.), 231  
Tremaine, S., & Weinberg, M.D. 1984, *ApJL*, 282, L5  
van Albada, G.D. 1985, *A&A* 142, 491  
van Albada, T.S., Bahcall, J.N., Begeman, K., & Sancisi, R. 1985, *ApJ*, 295, 305  
van Albada, T.S., & Sancisi, R. 1986, *Phil. Trans. Roy. Soc. Lond. A*, 320, 447  
van den Bosch, F.C. 1998, *ApJ*, 507, 601  
van den Bosch, F.C. 2000, *ApJ*, 530, 177  
van der Kruit, P.C. 1995, in *IAU Symposium 164, Stellar Populations*, ed. van der Kruit, P.C. & Gilmore, G., (Dordrecht: Kluwer), 205  
van der Kruit, P.C., & Searle, L. 1982, *A&A* 110, 61  
Weinberg, M.D. 1985, *MNRAS*, 213, 451  
Weiner, B.J., & Sellwood, J.A. 1999, *ApJ*, 524, 112  
Weiner, B.J., Williams, T.B., van Gorkom, J.H., & Sellwood, J.A. 2000, *ApJ* in press (Paper I)  
White, S.D.M., & Rees, M.J. 1978, *MNRAS*, 183, 341  
Zaritsky, D., Kennicutt, R.C., & Huchra, J.R. 1994, *ApJ*, 420, 87  
Zwaan, M.A., van der Hulst, J.M., de Blok, W.J.G., & McGaugh, S.S. 1995, *MNRAS*, 273, L35